universität wien

MASTERARBEIT | MASTER'S THESIS

Titel | Title

Construction and characterization of a single-electron detector with sub-micron resolution

verfasst von | submitted by

Luis Alfredo Ixquiac Méndez

angestrebter akademischer Grad | in partial fulfilment of the requirements for the degree of

Master of Science (MSc)

Wien | Vienna, 2026

Studienkennzahl lt. Studienblatt | Degree programme code as it appears on the student record sheet:	UA 066 876
Studienrichtung lt. Studienblatt | Degree programme as it appears on the student record sheet:	Masterstudium Physics
Betreut von | Supervisor:	Univ.-Prof. Dipl.-Ing. Dr. Thomas Juffmann

To my parents, René Alfredo Ixquiac Cabrera and Amelia Judith Méndez Flores,
my sister Virginia Judith Ixquiac Méndez,
and all my family,
with love and gratitude.

Contribution Statement

This thesis contains data published in the article:

Luis Alfredo Ixquiac Méndez, Martino Zanetti, Tilman Kräft, and Thomas Juffmann. Low-energy single-electron detector with submicron resolution. ACS Photonics, 2025.

The original research idea was proposed by Thomas Juffmann (T.J.).

My contribution to the article was as follows: design of the detector (lead together with T.J.), construction of the detector (lead), experimental implementation (lead), Monte Carlo simulations (lead), data acquisition and data analysis for detector characterization (lead), electron diffraction experiments at sub-millimeter sample–screen distances (no contribution), and preparation of the manuscript (majority of the initial draft; substantial written contributions and major revisions by co-authors).

All content presented in this thesis, including experiments, simulations, and data analysis, was performed by the author of this thesis. This thesis also contains data that is not published in any other journal.

Acknowledgements

First and foremost, I would like to thank my supervisor, Thomas Juffmann, for welcoming me into his group and for all of his support and guidance during the development of this project and during my studies.

Special thanks to Martino Zanetti for his crucial work on controlling the electron beam, and to Tilman Kräft for his important contribution in demonstrating the detector in diffraction experiments. I am also grateful to both of them for their fruitful discussions and valuable suggestions during the development of this project. I would like to thank Peter Kunnas for his initial guidance on the Monte Carlo simulations presented in this work. Additionally, I would like to thank Florian, Zdeněk, Ilia, Lucas G., Lucas K., Raphaël, Hanieh, Dante, Barbara, Clara, Alex, Vicky, Ivana, Floor, Constanza, Philipp, Felix, Sami, and Ugo for their valuable support during the development of this project.

I would also like to express my gratitude to all the people who supported me in beginning and continuing my studies in Vienna, especially Jani, Manuel, Kathrin, Susanne, Michael, and Thomas.

I would like to express my deepest gratitude to my parents, René Alfredo Ixquiac and Amelia Judith Méndez, whose support made it possible for me to fulfill my dream of continuing my studies abroad. I also want to thank my sister Virginia; my grandparents, Marcelo Ixquiac, Rosa Cabrera, Guillermo Méndez, and Amelia Flores; my uncles, Marcelo, Manuel, Moisés, and Milton Ixquiac, and Fernando and Sofía Méndez; and my dearest Sharon, Magdalena, and Ramiro. Their guidance, encouragement, and support have enabled me to reach where I am today.

I would also like to express my deepest thanks to Sarah and her family for welcoming me, supporting me, and making me feel at home in Austria.

Abstract

Single-electron detectors are crucial components of electron microscopes, electron spectroscopy setups, and electron optics experiments. This work presents a single-electron detector consisting of a scintillator on which electrons impinge, and the generated photons are collected by an optical system. The detector characteristics depend on the kinetic energy of the incident electrons. For 17 keV electrons, one achieves a spatial resolution estimate of 0.9 μm, derived from measurements and simulations. Electrons are identified with an efficiency and purity of 0.82 and 0.77, respectively. For 30 keV electrons, the spatial resolution estimate is 2.3 μm with efficiency and purity of 0.96 and 0.96, respectively.

Kurzfassung

Einzelelektronen-Detektoren sind essenzielle Komponenten von Elektronenmikroskopen, Elektronenspektroskopie-Setups und optischen Elektronenexperimenten. Diese Arbeit präsentiert einen Einzelelektronen-Detektor bestehend aus einem Szintillator, auf den Elektronen einwirken, und einem optischen System, das die generierten Photonen sammelt. Die Eigenschaften des Detektors sind abhängig von der kinetischen Energie der einfallenden Elektronen. Für 17 keV Elektronen, ist eine räumliche Auflösung von annähernd 0.9 μm zu erreichen, was von Messungen und Simulationen abgeleitet wird. Elektronen werden mit einer Effizienz und Reinheit von jeweils 0.82 und 0.77 ermittelt. Für 30 keV Elektronen liegt die räumliche Auflösung bei annähernd 2.3 μm, mit einer Effizienz und Reinheit von jeweils 0.96 und 0.96.

Contents

List of Figures

1 Introduction

Electron detectors are an important component of electron microscopes, electron spectroscopy setups, and electron optics experiments. These can be divided into two categories: scintillator-coupled detectors and direct detectors. Following [5], in a scintillator-coupled detector, electrons impinge on a scintillator, and the generated photons travel through a fiber optic coupling to a CCD or CMOS detector. In a direct detector, electrons impinge directly on a radiation-hardened sensor with a CMOS readout architecture. Direct detectors can be divided into two categories: hybrid pixel array detectors with pixel sizes typically of $55 \times 55\,\mu m$ [6] or larger [7], and monolithic active pixel sensors with pixel sizes down to $5\,\mu m$ [8, 9].

The detector presented in this work consists of a scintillator on which electrons impinge, and a portion of their kinetic energy is converted into luminescence emission of photons. These signals are imaged by an optical system, consisting of an oil immersion objective and a tube lens, onto the chip of a CMOS sensor. The acquired data is then processed, identifying the electron events.

This work demonstrates single electron detection and counting in an energy range between 17 keV and 30 keV, based on a Yttrium Aluminum Garnet doped with Cerium (YAG:Ce) scintillator ([10]). The detector characteristics depend on the kinetic energy of the incident electrons. For 30 keV electrons, an average of 26 photons are collected per electron event, obtaining an efficiency and purity in the classification of single-electron events of 0.96 and 0.96, respectively, and obtaining a spatial resolution estimate of $2.3\,\mu m$, derived from measurements and simulations. For 17 keV electrons, an average of 16.6 photons are collected per electron event, with efficiency and purity of 0.82 and 0.77, respectively, and a spatial resolution estimate of $0.9\,\mu m$.

The high spatial resolution of this detector enables electron diffraction studies at sub-millimeter distances between the sample and the detection screen, as it is demonstrated in [4]. Furthermore, it will enable more sensitive quantum electron optics experiments, such as ponderomotive wavefront shaping in a low-intensity limit [11, 12].

1.1 Structure of the thesis

This thesis is structured as follows.

Chapter 2 comprises four key topics that are necessary to understand the detection process of electrons by the electron detector that is presented in this work. How a portion of the kinetic energy of an incident electron can be transferred to the scintillator material is explained in the first part of section 2.1. The scintillation mechanism, explained in the second part of section 2.1, then explains how a portion of the absorbed energy is converted

into luminescence emission of photons. Section 2.2 explains the Binomial and Poisson distributions. The binomial distribution is used to understand the Poisson distribution, which is fundamental to understanding important noise sources of image sensors and, consequently, of this detector. Section 2.3 explains the fundamentals of the detection process of photons by a semiconductor image sensor together with its main noise sources. Lastly, section 2.4 explains the principles of binary classification, which are used in the processing of the data to identify the electron events.

Chapter 3 presents the results of a study of the dimensions of the space region from where the scintillated light, due to an incident electron, is emitted. This study is carried out with Monte Carlo simulations performed with the CASINO simulation software [13]. The results of these simulations play an important role in the data processing of the electron signals and in the estimation of the spatial resolution of the detector.

Chapter 4 explains the parts and construction process of the detector.

Chapter 5 explains the electron-detection process, delving into the data analysis for detection of events.

Chapter 6 presents the measurement results of the detector. In particular, the characteristics of the detector are presented as a function of the kinetic energy of the detected electrons.

Finally, Chapter 7 presents the conclusions of this work and proposals for further work to continue the development of the electron detector.

2 Theoretical background

2.1 The Scintillation Process

The scintillation process, due to the impingement of an electron on a scintillator crystal, can be divided into two consecutive stages:

1. interactions of the electron with the scintillator, in which a portion of the kinetic energy of the electron is absorbed by the scintillator;
2. the scintillation mechanism, in which a portion of the absorbed energy is converted into luminescence emission of photons.

These stages are now explained.

2.1.1 Interactions of electrons with matter

Following E. B. Podgorsak [1], when an electron travels through a material, it experiences Coulomb interactions with the orbital electrons and nucleus of the atoms in the material. These interactions can be classified in three categories, which are characterized by the size of the classical impact parameter b of the trajectory of the incident electron compared with the classic atomic radius a of the atom of the material with which the electron will interact (see Figure 2.1).

- When $b \approx a$, the electron may undergo a hard collision in which the electron may have a direct Coulomb interaction with a single atomic orbital electron. The orbital electron leaves the atom and has enough energy to undergo its own Coulomb interactions with other atoms. An electron experiences, in general, a small number of hard collisions as it travels through the material; however, the energy transfer associated with each hard collision is relatively high.
- When $b \gg a$, the electron may undergo a soft collision in which the electron interacts with the whole atom and its bound electrons. An electron in the valence band may be excited or even ionized. An electron experiences, in general, a large number of soft collisions as it travels through the material; however, the energy transfer associated with each soft collision is relatively small.
- When $b \ll a$, the electron may undergo a radiation collision in which the electron interacts mainly with the nucleus of the atom, and consequently, the electron is scattered by the nucleus. These interactions may be elastic or inelastic. In an elastic scattering, the kinetic energy loss of the electron is negligible. In an inelastic

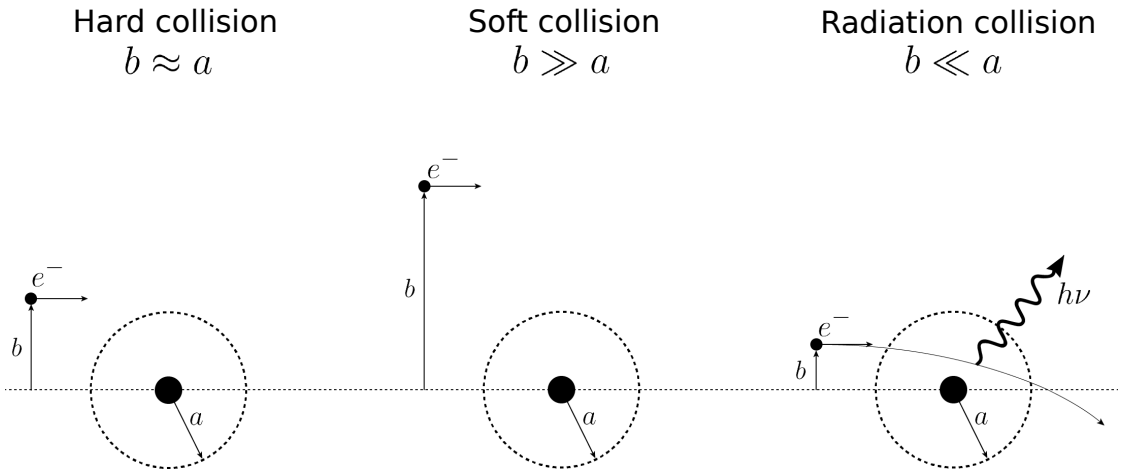

Figure 2.1: Three kinds of collisions of an electron with an atom: hard collision ($b \approx a$), soft collision ($b \gg a$), and radiation collision ($b \ll a$). Based on E. B. Podgorsak [1].

scattering, the electron emits x-ray photons, resulting in a significant kinetic energy loss for the electron, and the interaction is called a bremsstrahlung collision. The majority of these interactions are elastic.

2.1.2 The Scintillation Mechanism in Inorganic Crystals

This section follows closely the books of J. B. Birks [2] and G. F. Knoll [3].

A framework through which the scintillation mechanism can be explained is provided by the energy band model. The electronic energy states of an isolated atom or molecule consist of a set of discrete energy levels defined by Schrödinger's equation. An inorganic crystal lattice is a composite system where the interactions between atoms give rise to a modified electronic structure in such a way that the original energy levels of an isolated atom are broadened in a series of continuous energy bands, separated by forbidden regions of energy. These bands may be completely filled or empty. For an ideal insulating crystal that is in its ground state, its lowest energy band is completely filled. Its highest filled energy band is called the valence band, and its lowest empty band is called the conduction band. The separation between the valence band and the conduction band is called energy gap and is denoted by E_g. For instance, the energy gap of a yttrium aluminum garnet $Y_3Al_5O_{12}$ (YAG) crystal is $E_g = 8\,\mathrm{eV}$ [14].

Electrons are free to migrate through the bands. Notice that motion through a filled band does not imply that there is electrical conduction, since the fact that the band is filled implies that an equal number of electrons move in opposite directions. An electron in the valence band may be excited into the conduction band by the absorption of energy, leaving a hole in the valence band. One possible consequence of this is that the electron and hole are free to independently move in the conduction and valence bands, respectively. Another

possibility is that the excited electron remains bound to the positive hole. This system, called an exciton, possesses no net charge and is free to migrate throughout the crystal lattice. The exciton band corresponds to a band of energies below the conduction band. An exciton may also be formed by the recombination of an electron in the conduction band and a hole in the valence band.

In practice, a crystal is not perfect, and it might have impurities, interstitial ions, and interstitial defects. These create local discrete electronic energy levels, called centres, which locally modify the band structure of the pure crystal.

Consider an electron moving in the conduction band and a hole moving in the valence band such that they are in the vicinity of a centre. If the centre is unoccupied, this may be excited by the capture of both the electron from the conduction band and the hole from the valence band, either by simultaneously capturing an exciton or by the electron-hole recombining at the centre. When the centre is exited by the capture of both an electron and a hole, this creates a neutral configuration that has its own set of eexcitedstates. Moreover, when a centre is exited, there are three main scenarios that may happen (see Figure 2.2).

- If the excited state of the centre has an allowed transition to its ground state, its de-excitation may occur accompanied by photon emission. In this case the centre is called a luminescence centre or recombination centre. The typical lifetime of these excited states is on the order of $30 - 500\,\text{ns}$.

- The excitation energy of the centre is expended in radiationless thermal dissipation. In this case the centre is called a Quenching centre.

- The electron de-excites to a metastable level below the conduction band. Subsequently, the electrons may return to the conduction band by acquiring thermal energy from the lattice vibrations or fall to the valence band by a radiationless transition.

Luminescence centres are the basis of the scintillation mechanism. Notice that, in a pure crystal, the typical size of the energy gap E_g, is such that the de-excitation of an electron in the conduction band to the valence band would result in the emission of a high-energy photon that would not lie in the visible range. For instance, if the energy gap of the crystal is $E_g = 3\,\text{eV}$, the de-excitation of an electron back to the valence band would result in the emission of a photon of an energy of $3\,\text{eV}$, corresponding to a wavelength of $413\,\text{nm}$, which is close to the lower limit of the visible range. Thus, to improve the probability of visible photon emission, small amounts of properly chosen impurities, called activators, may be intentionally added to the inorganic crystals to create luminescence centres with energy levels such that their de-excitation is accompanied by the emission of photons in the visible range. Cerium is one example of an activator. The resulting crystal is called a Cerium-Activated crystal. A YAG crystal activated by Cerium is known as a YAG:Ce scintillator, which plays an important role in this work, as it is the scintillator used to detect the location of incident electrons.

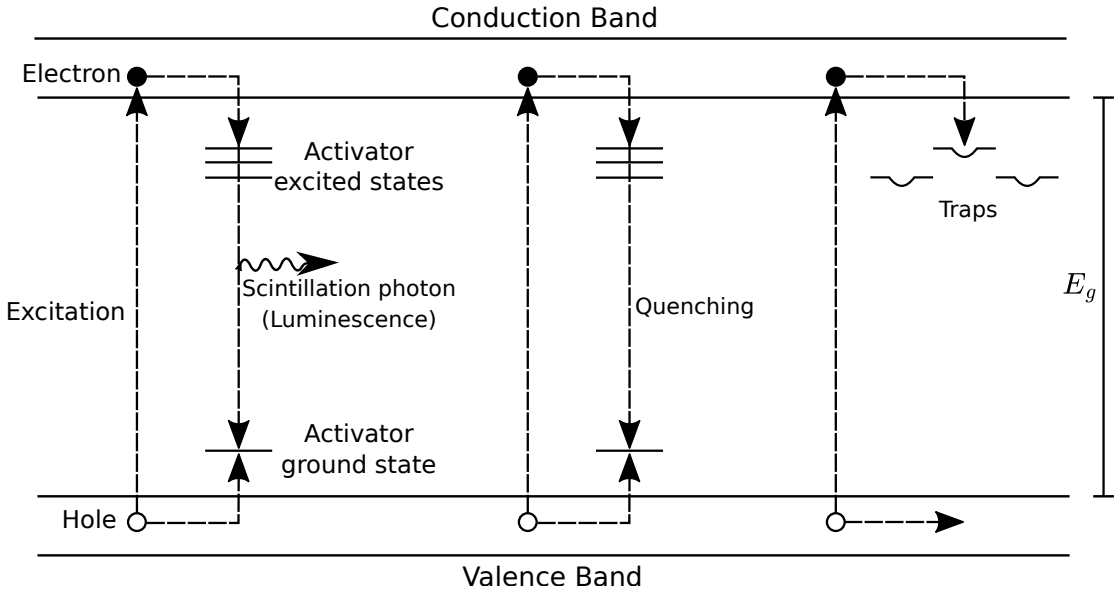

Figure 2.2: Schematic diagram of the energy band structure of an impurity-activated crystal, showing the excitation of an electron to the conduction band and the luminescence, quenching, and trapping scenarios. Based on J. B. Birks [2] and G. F. Knoll [3].

Consider a charged particle impinging on a scintillator crystal. As the electron travels through the material, a portion of its kinetic energy is absorbed by orbital electrons of the atoms in the scintillator. This will form a large number of electron-hole pairs. The migration time for the electrons and holes to excite the luminescence centres of the material is much shorter than the typical lifetime of the excited states of the luminescence centres. Thus, it is the decay time of the excited state of the luminescence centres that determines the time characteristics of the emitted light. For instance, the principal decay time of exited luminescence centres of Cerium, which depends on the host crystal, lies in the range $[20, 80]$ ns.

2.2 The Binomial and the Poisson distributions

This section follows closely the book of W. Feller [15].

2.2.1 The Binomial distribution

A process that has only two possible outcomes (success or failure), and such that the probabilities of these two outcomes are always the same (whenever such a process takes place) is called a Bernoulli trial.

Consider a Bernoulli trial. Let us denote the outcome "success" by S and the outcome "failure" by F. Moreover, let us denote by p the probability of obtaining S, and by q the

probability of obtaining F. Since there are only two possible outcomes, whenever the Bernoulli trial takes place, then

$$p + q = 1.$$

The possible outcomes of an individual Bernoulli trial are S and F. The possible outcomes of performing n Bernoulli trials can be described by 2^n successions of n symbols S and F. Then, the probability of any specified sequence is the product obtained by replacing the symbols S and F by p and q, respectively. This is, let $L = SSFF \dots SFSF$ be a sequence consisting of k successes and $n - k$ failures. The probability that the outcome of n consecutive Bernoulli trials is the sequence L is $P\{L\} = P\{SSFF \dots SFSF\} = ppqq \dots pqpq = p^k q^{n-k} = p^k(1-p)^{n-k}$. Notice that this probability depends only on the number of Bernoulli trials, the number of successes, and the probability of success, and it is independent of the order in which the successes and failures occur.

Consider the event $E \coloneqq$ "the outcome of n Bernoulli trials is k successes and $n - k$ failures." The probability that the outcome of n Bernoulli trials is a specified sequence that contains k successes and $n - k$ failures is $p^k(1-p)^{n-k}$. And the number of such sequences is the number of sequences that contain k symbols S and $n - k$ symbols F, which is given by the number of ways k elements can be chosen from a set of n elements (the set of n elements can be pictured as the set of numbers $\{1, \dots, n\}$ that represent the position of the symbols S or F in the sequence, and the chosen k numbers represent the location of the symbols S). Therefore, the number of such sequences is $\frac{n!}{k!(n-k)!}$. Thus the probability of the event E is

$$P(E) = \frac{n!}{k!(n-k)!} p^k (1-p)^{n-k}.$$

Let

$$b(k; n, p) \coloneqq \frac{n!}{k!(n-k)!} p^k (1-p)^{n-k}.$$

Then $b(k; n, p)$ is the probability that n Bernoulli trials with probability p for success and probability $(1 - p)$ for failure result in k successes and $n - k$ failures. $b(k; n, p)$ is called the binomial distribution.

Notice that $b(k; n, p)$ is the kth term of the binomial expansion of $(q+p)^n$ (this explains the name "binomial"). Since $p + q = 1$, then

$$1 = (q + p)^n = b(0; n, p) + b(1; n, p) + \cdots + b(n; n, p).$$

Notice that

$$\frac{b(k; n, p)}{b(k-1; n, p)} = \frac{(n - k + 1)p}{k(1-p)}.$$

2.2.2 The Poisson distribution approximation

Let $n \in \mathbb{N}$, and let $p = p(n) \in [0, 1]$. Let $\lambda \coloneqq np$. Moreover, suppose that for large n, $p(n)$ decreases small enough so that λ converges to a finite number.

Consider the binomial distribution

$$b(k;n,p) = \frac{n!}{k!(n-k)!}p^k(1-p)^{n-k}.$$

For $k = 0$, it takes the form

$$b(0;n,p) = (1-p)^n = \left(1 - \frac{\lambda}{n}\right)^n.$$

Taking the natural logarithm of both sides of this expression, one gets

$$\ln(b(0;n,p)) = n\ln\left(1 - \frac{\lambda}{n}\right).$$

Using the Taylor expansion $\ln(1-x) = -x - \frac{x^2}{2} - \frac{x^3}{3} - \cdots$, one gets

$$\ln(b(0;n,p)) = -\lambda - \frac{\lambda^2}{2n} - \cdots.$$

Thus, for large n, taking the exponential on both sides, one gets

$$b(0;n,p) \approx e^{-\lambda}.$$

Now, since n is large, and thus p is small, then, for any k we have that

$$\frac{b(k;n,p)}{b(k-1;n,p)} = \frac{(n-k+1)p}{k(1-p)} = \frac{\lambda - p(k-1)}{k(1-p)} \approx \frac{\lambda}{k}.$$

Thus, for $k = 1$,

$$b(1;n,p) \approx \lambda(0;n,p) \approx \lambda e^{-\lambda}.$$

For $k = 2$,

$$b(2;n,p) \approx \frac{\lambda}{2}b(1;n,p) \approx \frac{\lambda^2}{2}e^{-\lambda}.$$

In general, it can be shown by induction, that for any $k \in \{0,\ldots,n\}$,

$$b(k;n,p) \approx \frac{\lambda^k}{k!}e^{-\lambda}.$$

The function

$$p(k,\lambda) := \frac{\lambda^k}{k!}e^{-\lambda}$$

is called the Poisson distribution.

Notice that

$$p(0,\lambda) + p(1,\lambda) + p(2,\lambda) + \cdots = e^{-\lambda}(1 + \frac{\lambda^1}{1!} + \frac{\lambda^2}{2!} + \cdots) = e^{-\lambda}e^{\lambda} = 1.$$

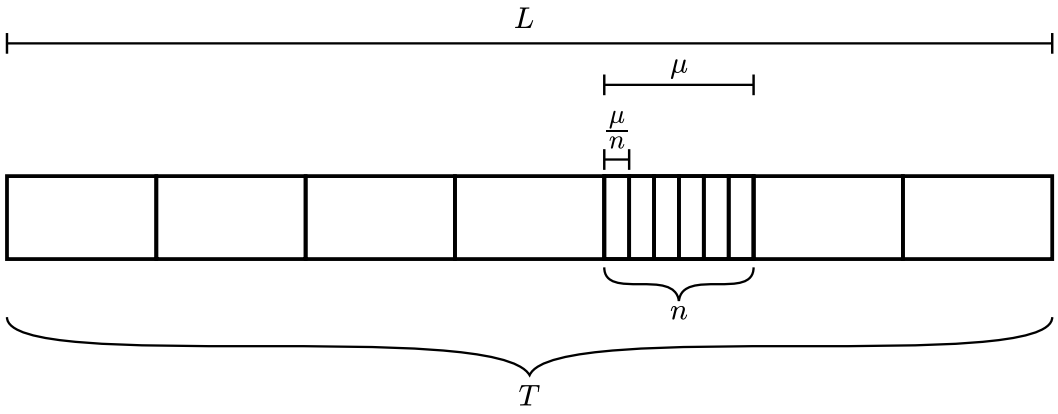

Figure 2.3: Representation of a region of size L divided into T regions of size μ each of which is further subdivided into n regions of size $\frac{\mu}{n}$.

2.2.3 Interpretation of the Poisson distribution

Let L denote the d-dimensional volume (size) of a d-dimensional region of space (see Figure 2.3). For instance, for $d = 1$ it can denote the length of a time interval or the length of a space interval, and for $d = 2$ it can denote the area of a region in a plane. Let us divide the region of size L into T regions, each of equal size $\mu = \frac{L}{T}$. Furthermore, each region of size μ, is further subdivided into n regions, each of equal size $\frac{\mu}{n} = \frac{L}{nT}$, so that the region of size L is subdivided into nT regions in total.

Now suppose that a point is randomly placed into the region L. Suppose that the probability the point lands in one specified region of the nT regions is $\frac{1}{nT}$. This is, the probability of appearance in any of the nT regions is the same.

In what follows, let us consider only one of the subregions of size μ. Furthermore, suppose that n points are randomly distributed into the full region L. Notice that each time a point is distributed along the region L, the probability of it landing on a specified region of size $\frac{\mu}{n}$ is always the same. This is, the probability of one point landing on a specified subregion of size $\frac{\mu}{n}$ is independent of where other points land.

Suppose that n is large enough so that the probability of having two points on a subinterval of length $\frac{\mu}{n}$ is negligible.

Then, the probability of having k points on this subregion of size μ is $b(k, n, p)$. Since n is large and p is small, then the Poisson approximation to the binomial distribution can be used. Let

$$\lambda = np = n\frac{1}{nT} = \frac{\mu}{L}.$$

Let $\tau \coloneqq \frac{1}{L}$, so that

$$\lambda = \tau\mu.$$

Thus,

$$b(k, n, p) = p(k, \lambda) = \frac{\lambda^k}{k!}e^{-\lambda}.$$

Thus, the probability of having k points on a specified subregion of size μ is given by

$$p(k, \tau\mu) = \frac{(\tau\mu)^k}{k!} e^{-\tau\mu}. \tag{2.1}$$

This is the interpretation of the Poisson distribution. In particular, the probability of having no point in a specified subregion of size μ is

$$p(0, \tau\mu) = e^{-\tau\mu}.$$

And the probability of having one or more points on a specified subregion of size μ is

$$1 - e^{-\tau\mu}.$$

Consider the event $H :=$ "n points are randomly distributed into the region L." Consider a fixed region of size μ. Suppose that this event H is observed for N times, and that each time that it is observed, one counts the number of of points that land in the specified region of size μ.

Each time the event H is observed, it happens that some number k of points land in the specified region of size μ. Let N_k be the number of times k points where observed. Since each time the event H is observed, there exist a k such that N_k will increase by 1, and since this is done N times, then

$$N_0 + N_1 + N_2 + \cdots = N.$$

Moreover, the total number of points that land in the specified interval of size μ after the N observations of the event H is

$$Q := 0N_0 + 1N_1 + 2N_2 + \cdots . \tag{2.2}$$

Then, the average number of points that land in the specified region of size μ is

$$\bar{k} = \frac{Q}{N}.$$

Moreover, since N is large, then

$$N_k \approx N \cdot p(k, \tau\mu) \tag{2.3}$$

Substituting (2.3) in (2.2), one gets

$$\begin{aligned}
Q &= 0N_0 + 1N_1 + 2N_2 + \cdots \\
&= N(1 \cdot p(1, \tau\mu) + 2 \cdot p(2, \tau\mu) + \cdots) \\
&= Ne^{-\tau\mu} \left(\frac{1(\tau\mu)}{1!} + \frac{2(\tau\mu)^2}{2!} + \frac{3(\tau\mu)^3}{3!} + \cdots \right) \\
&= Ne^{-\tau\mu}(\tau\mu) \left(1 + \frac{\tau\mu}{1!} + \frac{(\tau\mu)^2}{2!} + \cdots \right) \\
&= Ne^{-\tau\mu}(\tau\mu)e^{\tau\mu} \\
&= N(\tau\mu)
\end{aligned}$$

Thus,

$$\bar{k} = \frac{Q}{N} = \tau\mu = \lambda$$

is the mean of the Poisson distribution.

Moreover, it can be shown that the standard deviation of the Poisson distribution is

$$\sigma = \sqrt{\bar{k}} = \sqrt{\lambda}.$$

2.3 Semiconductor image sensors

This section follows closely the book of J. R. Janesick [16] and the white paper by Hamamatsu Photonics [17].

2.3.1 Detection process of a semiconductor image sensor

In the following, one possible mechanism for detecting an incident photon in a semiconductor image sensor is described.

An incident photon on a semiconductor can generate electron-hole pairs through the photoelectric effect. Once the electron-hole pairs have been created, the electrons are free to move in the semiconductor lattice. At the interior of the semiconductor, there is one region containing the pixel elements, which contains a charge detection element (see Figure 2.4). Moreover, this region possesses local electric fields that are engineered so that free electrons are not accelerated laterally but are accelerated straight to the closest pixel. In this way, a free electron that was created in the electric field region close to a pixel element is transported towards the pixel element and thus collected. An electron created in an electric field-free region may undergo random diffusion in all directions. It may either recombine or, if it reaches the electric field region, be transported to the corresponding charge collection element.

For silicon, the minimum required photon energy to free a valence electron is approximately $E = 1.14\,\text{eV}$. In terms of wavelength, this is

$$\lambda = \frac{12,390}{E}$$

where λ is the wavelength (Å) and E is the energy (eV) of the photon.

Thus, the maximum required photon wavelength to free a valence electron is approximately $\lambda = 10,864\,\text{Å} = 1086.4\,\text{nm}$. For photon energies below $1.14\,\text{eV}$ (wavelengths above $\lambda = 1086.4\,\text{nm}$) the photoelectric does not take place, and direct detection is not possible. Thus, the detection of photons is IR-limited by the silicon bandgap energy.

2.3.2 Quantum Yield gain and Quantum Efficiency

Notice that not all incident photons on the silicon will result in the production of electrons. An incident photon that interacts with the silicon and results in the production of electrons will be called an interacting photon.

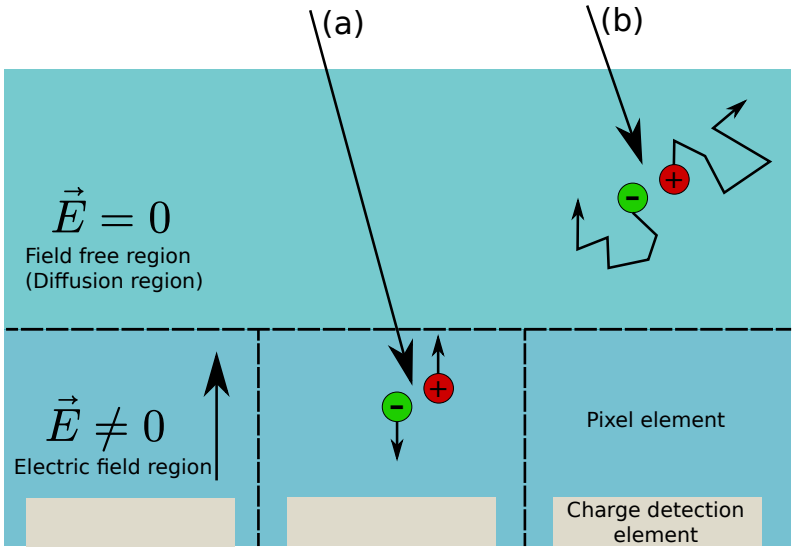

Figure 2.4: Schematic of the charge collection of electrons generated by incident photons: (a) an electron in the electric field region is transported to the charge collection element. (b) Charges in the field-free region undergo random diffusion in all directions. They may either recombine or, if an electron reaches the electric field region, it is transported to the charge collection element.

The Quantum Yield gain, denoted η, is the number of generated electrons per interacting photon (e^-/interacting photon).

For silicon, a single incident photon with energy in the range $[1.14, 3.1]\,\text{eV}$ can generate a single electron though the photoelectric effect. This energy range covers the wavelength regions of visible ($[400, 700]\,\text{nm}$) and near-IR ($[700, 1100]\,\text{nm}$). A photon with energy greater than approximately $3.1\,\text{eV}$ will produce multiple electrons since the resulting photoelectron is energetic enough to undergo further collisions with other electrons in the lattice, which in turn can become free electrons. Notice then that the Quantum Yield gain can be greater than unity.

Let P denote the average number of incident photons per second per pixel (incident photons/s px) and P_I the average number of interacting photons per second per pixel (interacting photons/s px). The interacting Quantum Efiiciency, denoted by QE_I, is defined by

$$QE_I = \frac{P_I}{P}.$$

The interacting Quantum Efficiency is always less than unity and represents the fraction of incident photons that interact with the semiconductor.

and it is a figure of merit of how much incident photons are allowed to interact with the semiconductor.

The Quantum Efficiency, denoted by QE, and defined by

$$QE = \eta \cdot QE_I$$

represents the number of generated electrons per incident photon (e^-/incident photon). Notice that since the Quantum Yield gain can be greater than unity, then the Quantum efficiency can also be greater than unity.

The average number of photoelectrons per second per pixel ($e^-/\mathrm{s\,px}$) as a function of the average number of incident photons per second per pixel is given by

$$N_R = \eta \cdot P_I = \eta \cdot QE_I \cdot P = QE \cdot P.$$

Consider an observation time τ. The average number of photoelectrons, during the observation time τ, per pixel (e^-/px) is guiven by

$$N = \eta \cdot P_I \cdot \tau = \eta \cdot QE_I \cdot P \cdot \tau = QE \cdot P \cdot \tau.$$

2.3.3 Noise sources in semiconductor photosensors

The following presents three main noise sources that limit the performance of semiconductor photosensors. These are Photon shot noise, Dark current noise, and Readout noise.

Photon shot noise

Consider a source that emits photons randomly in space and time and independently of each other. Thus, the number of photons emitted during a fixed time interval is described by a Poisson distribution. An example of such a source is a coherent light source, which is physically well approximated by a single-mode laser.

The emitted photons described by a Poisson distribution can experience losses when traveling to the region of the semiconductor that contains the pixel elements. These losses can be due to optical apertures, filters, diffusers, absorbers, or diffractive elements. If these losses are described by a physical selection process that is completely random, then the amount of photons that manage to reach each specified region of a pixel element will again be described by a Poisson distribution. Therefore, the amount of photoelectrons collected by each specified pixel element, during a specified observation time τ, is described by a Poisson distribution. The standard deviation of the distribution of the number of photoelectrons collected by a pixel element (i, j), during a specified observation time τ, is called photon shot noise of the pixel $\sigma_{P_{ij}}$ (e^-/px). Since this distribution is a Poisson distribution, then the shot noise can be expressed as

$$\sigma_{P_{ij}} = \sqrt{N_{ij}}$$

where N_{ij} is the average number of photoelectrons, during the observation time τ, that arrive at the pixel (i, j).

Dark current noise

Suppose that the semiconductor photosensor is isolated from external photon sources. Thus, there are no incident photons that could potentially generate photoelectrons to be

collected by the pixel elements. However, the photoelectric effect is not the only process that can generate electron-hole pairs. The necessary energy for the creation of electron-hole pairs can be supplied by thermal energy of the semiconductor, i.e., sufficiently strong semiconductor lattice vibrations. An electron generated by this process will be called a thermally generated electron. Notice that the signal generated due to the collection of a thermally generated electron is indistinguishable from the signal generated by a photoelectron generated by an incoming photon.

The current density of thermally generated electrons, also called dark current density, is given by

$$j = (2.55 \times 10^{15}) \cdot D_{FM} \cdot T^{3/2} e^{-E_g/(2\kappa T)},$$

where D_{FM} is the dark current figure-of-merit at 300 K ($\mathrm{nA/cm^{-2}}$), which varies depending on the sensor manufacturer, κ is the Boltzmann's constant ($8.62 \times 10^{-5}\,\mathrm{eV/K}$), and E_g is the silicon bandgap energy, in eV, given as

$$E_g = 1.557 - \frac{(7.021 \times 10^{-4}) \cdot T^2}{1108 + T}.$$

The average number of thermally generated electrons per second per pixel ($e^-/\mathrm{s\,px}$), in terms of the dark current density j, is given by

$$D_R = \frac{j \cdot P_A}{q_e}$$

where P_A is the pixel area ($\mathrm{cm^2}$) and q_e is the elemental charge.

Consider an observation time τ. The average number of thermally generated electrons, during the observation time τ, per pixel (e^-/px) is given by

$$D = D_R \cdot \tau.$$

Notice that the thermal generation of electrons is a random process. The number of thermally generated electrons during a specified observation time τ in a specified region of a pixel element is thus described by a Poisson distribution. The standard deviation of the distribution of the number of thermally generated electrons collected by a pixel element (i, j), during a specified observation time τ, is called dark current noise of the pixel element $\sigma_{D_{ij}}$ (e^-/px). Since this distribution is a Poisson distribution, then the dark current noise can be expressed as

$$\sigma_{D_{ij}} = \sqrt{D_{ij}}$$

where D_{ij} is the average number of thermally generated electrons, during the observation time τ, at the pixel (i, j). Notice that, in general, the dark current noise can vary from pixel to pixel.

Readout noise

Consider the case of a CMOS image sensor. In this scenario, each pixel element possesses an electronic circuit for charge detection. The electronic circuit consists of a voltage follower, where a change in input voltage creates the same change at the output. At the input of the circuit, there is an effective capacitance C. When the photocharge Q reaches this capacitance, a voltage increase V given by

$$V = \frac{Q}{C}$$

occurs, and this is read out at the output of the circuit. However, this circuit exhibits thermal noise, and thus the output voltage is subject to noise. Hence, the measurement of the charge Q also exhibits thermal noise. The standard deviation of the charge detection process, at the pixel element (i, j), measured in electrons (e^-), and denoted by $\sigma_{R_{ij}}$, is called readout noise of the pixel element (i, j).

It is important to notice that the number of collected electrons by a specified pixel element (i, j) is described by a discrete-variable distribution, i.e., a distribution whose domain consists of natural numbers $\{0, 1, 2, \dots\}$. The measurement of this number is performed by measuring the output voltage of the electronic circuit, and this voltage output is affected by the noise of the electronic circuit. According to [18, 19], the noise of the electronic circuit is modeled by a continuous normal distribution. Thus, the measured number of electrons collected by the specified pixel element in general will no longer be a natural number. For instance, if the pixel element collects 3 electrons, then the measured number of electrons could be either 3.65 or 2.80 or 3.00. Thus, the measured number of collected electrons is modeled by the continuous distribution obtained by the convolution of the discrete-variable distribution (of the number of collected electrons) with the continuous normal distribution (modeling the noise of the electronic circuit). A plot of the discrete-variable distribution of the number of collected electrons by the pixel element can be pictured as a set of discrete peaks located at each natural number. For a small readout noise ($\sigma_{R_{ij}} = 0.3$ for instance) the continuous distribution of the measured number of collected electrons would look like the original discrete-variable distribution but smeared out into a continuous function with distinguishable peaks at each natural number.

A small readout noise of a pixel element (i, j) is an important characteristic for performing photon number resolving measurement at that pixel. Since each photocharge measurement is affected by the statistical uncertainty of the readout noise $\sigma_{R_{ij}}$, if this readout noise is, for instance, $\sigma_{R_{ij}} = 0.9$ electrons, then it is possible that a measurement of seven counts can be misclassified as six counts or as eight counts. According to [17], a readout noise of $\sigma_{R_{ij}} = 0.3$ electrons or less is required to correctly classify the photoelectron number in more than 90 % of the photodetection events, provided that losses due to non-unity quantum efficiency are not the dominant source of error.

In a CMOS image sensor, each pixel element has its own electronic circuit for charge detection. The readout noise of each pixel element may vary across the chip, i.e., each pixel element has its characteristic value of standard deviation of normal distribution

characterizing the noise of its electronic circuit for charge detection (the existence of pixels with high and low values of readout noise leads to visually dark and bright spots, which is called "salt and pepper noise"). Consider now the distribution of values of readout-noise of the pixels. The median and the root mean square of this distribution are figures of merit that characterize the readout noise of the whole chip. The readout noise of the camera chip is defined as the root mean square of the values of readout-noise of the pixels, and it is denoted by

$$\sigma_R \quad \text{(rms)}.$$

Dynamic range and Signal to noise ratio

Consider a pixel element (ij). The maximum charge that can be detected by the charge detection circuit of the pixel element, denoted $N_{max\,ij}$, and measured in electrons, is called Full Well Capacity of the pixel element. The dynamic range of the pixel element, denoted by DR_{ij}, is defined as

$$DR_{ij} = \frac{N_{max\,ij}}{\sigma_{R_{ij}}}.$$

Consider an observation time τ. The total noise of the pixel element, denoted by σ_{ij} is given by

$$\sigma_{ij} = \sqrt{\sigma_{P_{ij}}^2 + \sigma_{D_{ij}}^2 + \sigma_{R_{ij}}^2} = \sqrt{N_{ij} + D_{ij} + \sigma_{R_{ij}}^2}.$$

The signal-to-noise-ratio of the pixel element, denoted by SNR_{ij}, is defined as

$$SNR_{ij} = \frac{N_{ij}}{\sigma_{ij}} = \frac{N_{ij}}{\sqrt{N_{ij} + D_{ij} + \sigma_{R_{ij}}^2}} = \frac{QE \cdot P \cdot \tau}{\sqrt{QE \cdot P \cdot \tau + D_{ij} + \sigma_{R_{ij}}^2}}.$$

2.4 Binary classification

This section presents standard concepts and metrics for binary classification in the author's own style, following the definitions in [20].

Consider the sets

$$N \coloneqq \{n_1, n_2, n_3, \dots\}$$

and

$$P \coloneqq \{p_1, p_2, p_3, \dots\}.$$

Consider the set

$$S \coloneqq N \cup P.$$

An element $n \in N$ will be called an actual negative, and an element $p \in P$ will be called an actual positive.

Let $B : S \to \{0, 1\}$ be any specified function. This function B will be called a binary classification of the elements of the set S. The function B defines the sets

$$N' \coloneqq B^{-1}(\{0\})$$

and

$$P' \coloneqq B^{-1}(\{1\}),$$

which form a partition of the set S, this is, they don't possess elements in common and their union is the set S, this is

$$S = N' \sqcup P'.$$

An element $n' \in N'$ will be called a classified negative, and an element $p' \in P'$ will be called a classified positive.

Consider the function

$$E : S \to \{0,1\}, \qquad s \mapsto \begin{cases} 0, & s \in N, \\ 1, & s \in P. \end{cases}$$

This function E is such that $N' = N$ and $P' = P$, i.e. every element $s \in S$ that is classified negative is an actual negative, and every element $s \in S$ that is classified positive is an actual positive. The function E is thus a binary classification with a perfect performance in the task of properly classifiing the elements of the set S into their actual category. We will now define figures of merit that quantify the performance of a binary classification.

Let B be a specified binary classification. The binary classification B defines the following four disjoint sets:

$$\begin{aligned} TP \coloneqq P' \cap P &= \{\, s \in S : s \text{ is classified positive and is an actual positive} \,\} \\ &\quad \text{called set of true positives,} \\ FP \coloneqq P' \cap N &= \{s \in S : s \text{ is classified positive and is an actual negative}\} \\ &\quad \text{called set of false positives,} \\ TN \coloneqq N' \cap N &= \{s \in S : s \text{ is classified negative and is an actual negative}\} \\ &\quad \text{called set of true negatives,} \\ FN \coloneqq N' \cap P &= \{s \in S : s \text{ is classified negative and is an actual positive}\} \\ &\quad \text{called set of false negatives.} \end{aligned}$$

If A is a set let us denote its cardinality by $|A|$.

Using the definitions of TP, FP, TN, FN and the distributive law

$$A \cap (B \cup C) = (A \cap B) \cup (A \cap C),$$

it can be shown that

$$P = TP \sqcup FN$$

$$N = FP \sqcup TN,$$

hence,

$$|P| = |TP| + |FN|$$

$$|N| = |FP| + |TN|.$$

Let $\mathrm{CM}(B)$ denote the 2×2 matrix defined by

$$\mathrm{CM}(B) \coloneqq \begin{array}{c|cc} & \text{classified positive} & \text{classified negative} \\ \hline \text{actual positive} & |TP| & |FN| \\ \text{actual negative} & |FP| & |TN| \end{array}$$

This matrix $\mathrm{CM}(B)$ is called the confusion matrix of the binary classification B.

With the four defining numbers of $\mathrm{CM}(B)$, namely $|TP|$, $|FP|$, $|TN|$, $|FN|$, one can define the following eight ratios:

$TPR(B) \coloneqq \frac{\lvert TP\rvert}{\lvert TP\rvert+\lvert FN\rvert}$	$FNR(B) \coloneqq \frac{\lvert FN\rvert}{\lvert TP\rvert+\lvert FN\rvert}$
$TNR(B) \coloneqq \frac{\lvert TN\rvert}{\lvert TN\rvert+\lvert FP\rvert}$	$FPR(B) \coloneqq \frac{\lvert FP\rvert}{\lvert TN\rvert+\lvert FP\rvert}$
$PPV(B) \coloneqq \frac{\lvert TP\rvert}{\lvert TP\rvert+\lvert FP\rvert}$	$FDR(B) \coloneqq \frac{\lvert FP\rvert}{\lvert TP\rvert+\lvert FP\rvert}$
$NPV(B) \coloneqq \frac{\lvert TN\rvert}{\lvert TN\rvert+\lvert FN\rvert}$	$FOR(B) \coloneqq \frac{\lvert FN\rvert}{\lvert TN\rvert+\lvert FN\rvert}$

These are called, respectively, true positive rate (TPR), false negative rate (FNR), true negative rate (TNR), false positive rate (FPR), positive predictive value (PPV), false discovery rate (FDR), negative predictive value (NPV), and false omission rate (FOR). These ratios are figures of merit of the performance of the binary classification function B.

Notice that the two ratios on each row of the above table are complements of each other and they thus represent essentially the same information. The performance of the binary classification is described by the values of two independent ratios. The choice of this pair of rations depends on the application. Each of the eight ratios might have more than one name in the literature. In the context of this work —detection of electron events— the pair of ratios used to describe the performance of a binary classification are:

- the efficiency $\eta = TPR$, which describes the proportion of all actual positive events that are classified positive, and
- the purity $p = PPV$, which describes the proportion of all classified positive events that are actual positive.

Notice that $\eta, p \in [0, 1]$, and the closer both of them are to 1, the better the performance of the binary classification.

In terms of η and p, one can also define a single value which is a figure of merit of the performance of the binary classification. This is called the F_1-score, and is defined as

$$F_1 \coloneqq \frac{2\eta p}{\eta + p}.$$

Notice that $F_1 \in [0, 1]$, and the closer it is to 1, the better the performance of the binary classification.

Notice that, for the perfect binary classification function E,

$$\mathrm{CM}(E) \coloneqq \begin{bmatrix} |P| & 0 \\ 0 & |N| \end{bmatrix}.$$

Hence,

$$\eta(E) = \frac{|TP|}{|TP| + |FN|} = \frac{|TP|}{|TP|} = 1,$$

and

$$p(E) = \frac{|TP|}{|TP| + |FP|} = \frac{|TP|}{|TP|} = 1,$$

and therefore,

$$F_1(E) = 1.$$

In practice one knows the objects of the set S, but one does not know the actual classification of each of the elements $s \in S$, i.e., for each $s \in S$, whether it is an actual positive ($s \in P$) or whether it is an actual negative ($s \in N$). The goal is to classify the elements of the set S into their actual categories. This can be achieved by defining a suitable binary classification function B. In practice, for each $s \in S$ one might know k characteristics $(q_1(s), q_2(s), \dots q_k(s))$ of it. These can be numerical values, for instance. This can allow us, for each $s \in S$, to define the image value of B at s ($B(s)$) in terms of the k characteristics of the object s $(q_1(s), q_2(s), \dots q_k(s))$, this is,

$$B(s) \coloneqq \beta(q_1(s), q_2(s), \dots q_k(s)),$$

where

$$\beta : Q^k \to \{0, 1\}$$

is a function that takes as input k-tuples of elements of the set Q, which can be, for instance, a set of numbers (natural, real, or complex, for instance).

In what follows the function β will be denoted by B, this is $\beta = B$ (notation).

In practice, one might know that the defining characteristics of an $s \in N$ behave differently than the defining characteristics of an $s \in P$. This could allow to find a meaningful definition of the binary classification function B which would allow us to properly classify the elements of S into their actual category.

Examples of characteristics that the elements of the set S can have are:

- In a simple scenario, each element $s \in S$ has a single characteristic given by a real number $q(s)$.
- If each element $s \in S$ is an $l \times l$ image with pixel values in the natural numbers, then each element $s \in S$ has as $k = l \times l$ characteristics the $l \times l$ pixel values.
- If each element $s \in S$ is a physical object, it could be characterized by its physical properties like mass, charge, temperature, volume, etc.

In what follows, the explanation will focus on the first of the above three examples. This is, each element $s \in S$ has a single characteristic given by a real number $q(s)$.

Suppose the following:

- We are given a set of elements S, such that each $s \in S$ is characterized by a real number $q(s) \in \mathbb{R}$.
- Each element $s \in S$ belongs either to the category N or to the category P, and we want to find for each $s \in S$ to which category it actually belongs.
- We know that the possible characteristic values of the elements of the category N are described by the probability distribution F, and the possible characteristic values of the elements of the category P are described by the probability distribution G.
- The distributions F and G are such that F is predominantly concentrated at lower values than G.
- There is a large number $|N|$ of elements of the category N and a large number $|P|$ of elements of the category P (the exact number of elements in each category is information that in practice we initially do not know). What we do know in practice is the set S and for each $s \in S$, its value $q(s) \in \mathbb{R}$.

The fact that the values of the elements of S come either from the distribution F or G implies that the histogram of the values of the elements of the set S is a linear combination of the functions F and G. This can allow us to fit this histogram with a function of the form $aF + bG$ $(a, b \in \mathbb{R})$. With this information, the number of actual negatives can be estimated as

$$|N|_e = \int_{-\infty}^{\infty} aF$$

and the number of actual positives can be estimated as

$$|P|_e = \int_{-\infty}^{\infty} bG.$$

Moreover, as binary classification function, we can use the step function with threshold $T \in \mathbb{R}$,

$$B_T : \mathbb{R} \to \{0, 1\}, \qquad x \mapsto \begin{cases} 0, & x < T, \\ 1, & x \geq T. \end{cases}$$

Notice that each choice of threshold $T \in \mathbb{R}$ defines a binary classification function B_T.

With this information the number of true positives, false positives, true negatives and false negatives can be estimated as

$$|TP|_e = \int_T^\infty bG$$
$$|FP|_e = \int_T^\infty aF$$
$$|TN|_e = \int_{-\infty}^T aF$$
$$|FN|_e = \int_{-\infty}^T bG.$$

Furthermore, with these numbers the corresponding efficiency $\eta(T)$, purity $p(T)$ and F_1-score $F_1(T)$ of the binary classification B_T, determined by the threshold $T \in \mathbb{R}$, can be computed. The curve

$$c : \mathbb{R} \to [0,1] \times [0,1], \qquad T \mapsto (\eta(T), p(T))$$

will be called efficiency-purity curve. It plots, for each $T \in \mathbb{R}$ the performance of the binary classification B_T. It therefore gives a general overview of the different performances that can be achieved by the family of binary classification functions $\{B_T : T \in \mathbb{R}\}$.

3 Monte Carlo Simulations

We study the dimensions of the space region where the scintillated light of an electron event is emitted with a Monte Carlo simulation performed using the CASINO simulation software [13].

To generate a simulation, we need to define three main components, namely, the sample with which the electrons will interact, the electron beam characteristics, and the physics models. The parameters of each component are described below.

- Sample: As will be explained in section 4.1, in order to maximize the light collection efficiency, the scintillator possesses a 25 nm Al coating on the vacuum-facing surface, which acts as a mirror for the scintillated light (see Figure 3.1). The sample thus consists of the scintillator and the Al coating, and is modeled using two boxes. The first box defines the Al layer and has dimensions $(10000 \times 10000 \times 30)\,\mathrm{nm}^3$, and a density of $2.7\,\mathrm{g/cm}^3$. The thickness of the Al layer in the simulation is slightly increased with respect to the experimental value of 25 nm in order to provide a conservative upper bound on the effect of the Al layer on electron spreading. The second box defines the YAG:Ce scintillator and has dimensions $(10000 \times 10000 \times 10000)\,\mathrm{nm}^3$, and a density of $4.55\,\mathrm{g/cm}^3$. Following the instructions of the software [13], a very small empty gap of 1 nm is placed between the Al and YAG:Ce boxes to guarantee a correct update of the electron region each time the electron crosses the surfaces of the boxes.

- Electron beam: The simulation models 7×10^5 electrons impinging at a right angle on the Al coating surface on top of the YAG:Ce scintillator. The incident electrons move in the $+z$ direction. The xy plane is parallel to the external surface of the aluminum, where the electrons impinge. Different simulations are performed, each with electrons having a fixed kinetic energy within the range $[1, 30]\,\mathrm{keV}$.

- Physics models: The different steps and physical models used by CASINO to simulate electron trajectories are described in [21, 13, 22]. An electron trajectory is described by discrete elastic scattering events, and the inelastic events are approximated by a mean energy loss model between two elastic scattering events. The average distance between two successive elastic events is obtained from the total elastic cross-section, and a random number is used to distribute the distance following a probability distribution. The elastic scattering angle is obtained from another random number and using the differential elastic cross-section, which can be calculated using analytical models or tabulated values.

  Among the physics models provided by the software, the following are used. For the total and partial cross sections, Mott by interpolation is used. The random number

generator is Lagged Fibonacci. The stopping power is calculated using Joy and Luo + Lowney.

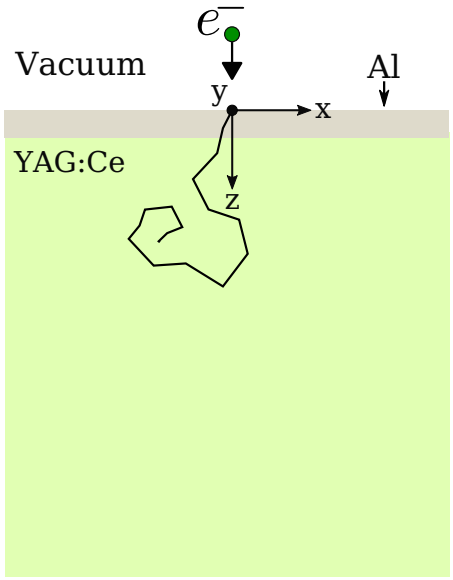

Figure 3.1: Sketch of the simulation setup. The interaction sample consists of the YAG:Ce scintillator together with the Al coating. Electrons impinge at a right angle on the external Al coating surface. The incident electrons move in the $+z$ direction, and the xy plane is parallel to the external surface of the Al coating.

Figure 3.2 below shows the XZ-projection of trajectories of 30 (green), 20 (blue), and 10 (purple) keV incident electrons.

For each electron, the simulation gives the kinetic energy of the electron at each position along its trajectory. This is, each electron trajectory consists of N points $((x_i, y_i, z_i) : i \in \{1, \ldots, N\})$, and for each $i \in \{1, \ldots, N\}$, E_i is the kinetic energy of the electron when it is at position (x_i, y_i, z_i). For each electron trajectory, it is calculated its position of center of energy loss given by

$$r_{\text{coel}} = (x_{\text{coel}}, y_{\text{coel}}) := \frac{\sum_{i=2}^{N}(x_i, y_i) \cdot (E_{i-1} - E_i)}{E_1}$$

This is, the position of center of energy loss is given by the weighted, by energy loss, average of the positions of each portion of the electron trajectory.

Thus, for each simulated electron, there is a position of incidence at the scintillator $r_{\text{in}} = (x_{\text{in}}, y_{\text{in}})$ and a position of center of energy loss of the scintillated electron signal r_{coel}. For each electron trajectory, the distance between these two positions, denoted by d_{ic}, is calculated.

In what follows, consider 30 keV incident electrons. Figure 3.3 shows four examples of trajectories (solid green lines), together with their corresponding positions of incidence r_{in}

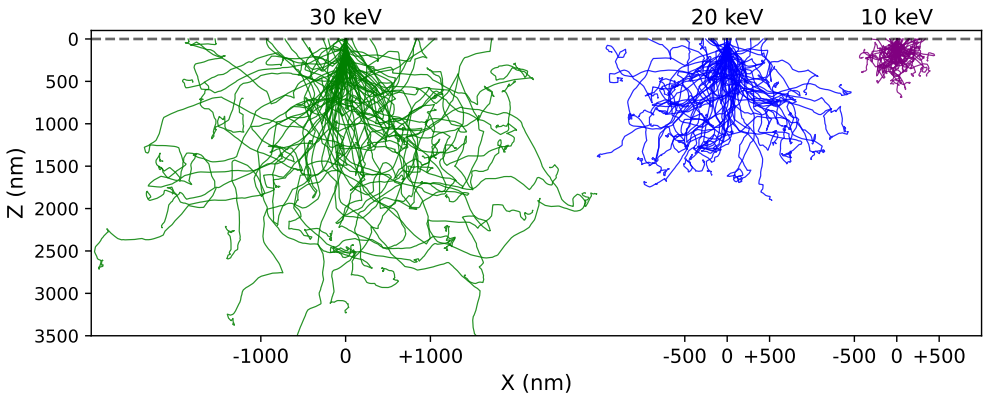

Figure 3.2: XZ-projection of trajectories of 30 (green), 20 (blue), and 10 (purple) keV incident electrons on the YAG:Ce scintillator. For each energy, 70 trajectories are plotted.

(blue circle) and center of energy loss r_{coel} (red circle), and the distance between these d_{ic}. The position of incidence r_{in} represents the real detection position of the electron, and the position of center of energy loss r_{coel} represents the measured position of detection of the electron when performing the data analysis. As the examples in figure 3.3 show, the distance d_{ic} between the positions r_{in} and r_{coel} can take different values depending on the trajectory that the electron followed in the material. Therefore, when measuring the position of an electron (r_{coel}), it has to be taken into account that its real position of incidence (r_{in}) might be at some distance d_{ic} away from this measured distance. In order to account for this, one calculates the median of all distances d_{ic}, denoted by $\tilde{d}_{ic}$.

Figure 3.4c shows the histogram (light blue) of the distances d_{ic} of all trajectories of 30 keV incident electrons. The median of these distances is $\tilde{d}_{ic} = 1009\,\text{nm}$. This value is taken into account when computing an estimate of the spatial resolution of the detector at 30 keV.

Furthermore, with the Monte Carlo simulations, one also calculates the average size of the space region where the scintillated light of an electron is emitted. This value serves as a reference for the spatial size of the electron signal and is used to localize the positions of the electron signals, as will be explained in Chapter 5. The average size of this space region is obtained by studying the average spatial distribution of energy loss of the electrons in the scintillator. The spatial distribution of energy loss is obtained by aligning all electron trajectories with respect to their coordinates of center of energy loss. Each segment of an electron trajectory contributes locally to the energy deposited at its corresponding position in the scintillator. Considering all trajectory segments, one obtains a spatial distribution of energy loss by the electrons in the scintillator. To visualize the results, the distribution is projected along the y-axis and then normalized with respect to the total energy loss by all electrons, thus obtaining its normalized xz projection, which is shown in Figure 3.4b together with 4 level curves, each containing 25, 50, 75, and 90 % of the total energy loss within them. Similarly, the distribution is projected along the z

axis and then normalized, thus obtaining its normalized xy projection which is shown in Figure 3.4a together with 4 level curves (circles by symmetry), each containing 25, 50, 68, and 90 % of the total energy loss within them. We interpret this normalized energy loss distribution due to all the electrons as the average energy loss distribution due to a single electron. Moreover, we approximate the average distribution of scintillated photons, due to an incident electron, to be proportional to this average energy loss distribution.

Inspection of the level curves of the normalized xy projection of the energy loss distribution indicates that 68 % of the scintillated photons, due to an incident electron, are emitted from a spatial region contained in a circle of radius $\sigma_G = 711\,\text{nm}$. This value of σ_G is later used in the data analysis for the detection of 30 keV incident electron events.

The simulation is performed for different values of kinetic energy in the range of $[1\,\text{keV}, 30\,\text{keV}]$. As a function of the kinetic energy of the incident electrons, Figure 3.4d shows the corresponding values of σ_G (purple dots) and $\tilde{d}_{ic}$ (blue squares).

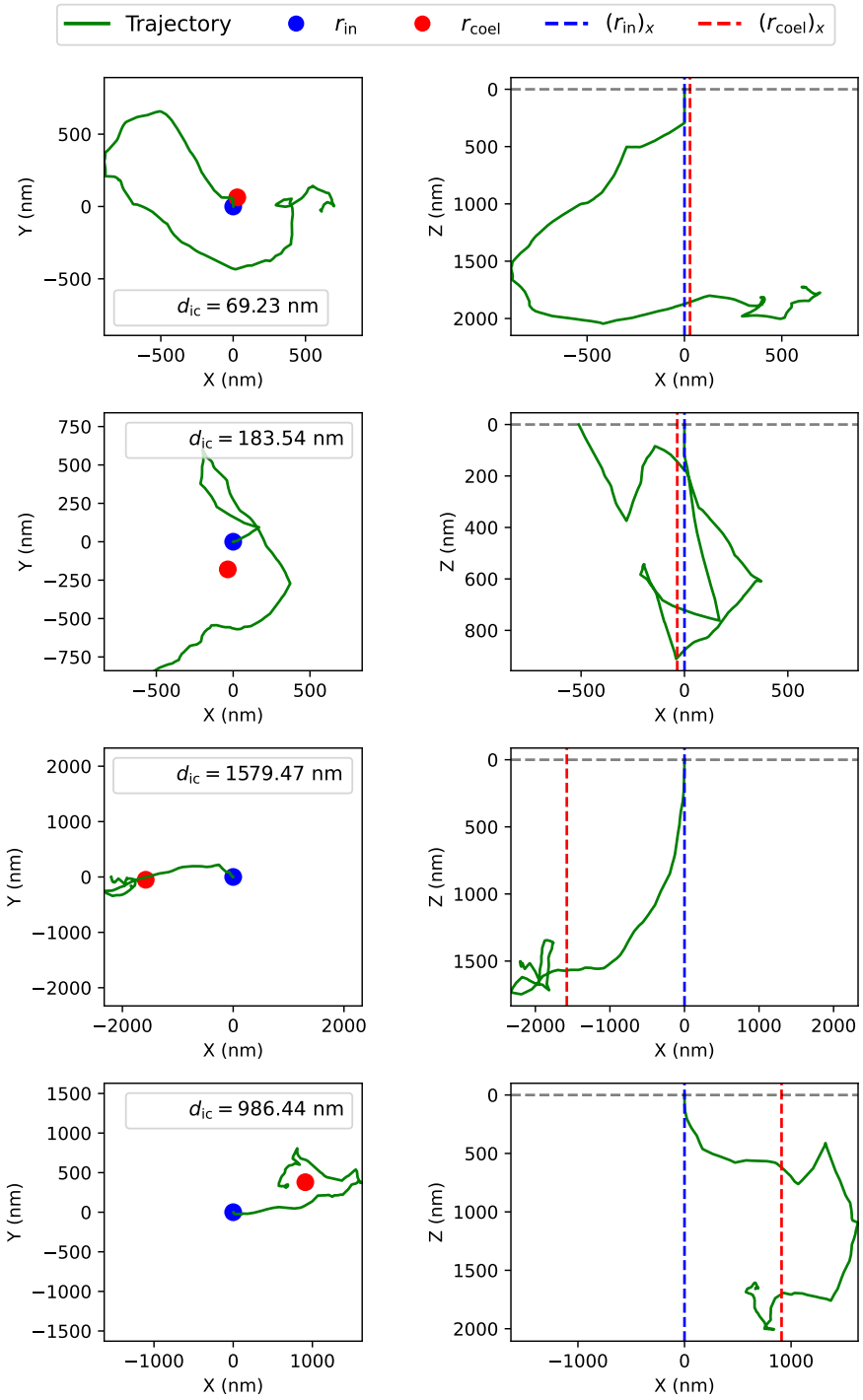

Figure 3.3: Four trajectories of 30 keV incident electrons. Each trajectory (solid green line) is represented by two plots on each row. These are its xy (left column) and xz (right column) projections. For each trajectory, its corresponding position of incidence r_{in} (blue circle) and center of energy loss r_{coel} (red circle) are shown on its xy projection, and the corresponding x coordinates of these positions (blue and red dashed lines) are shown on the corresponding xz projection. On each xy projection, the value of d_{ic} is shown.

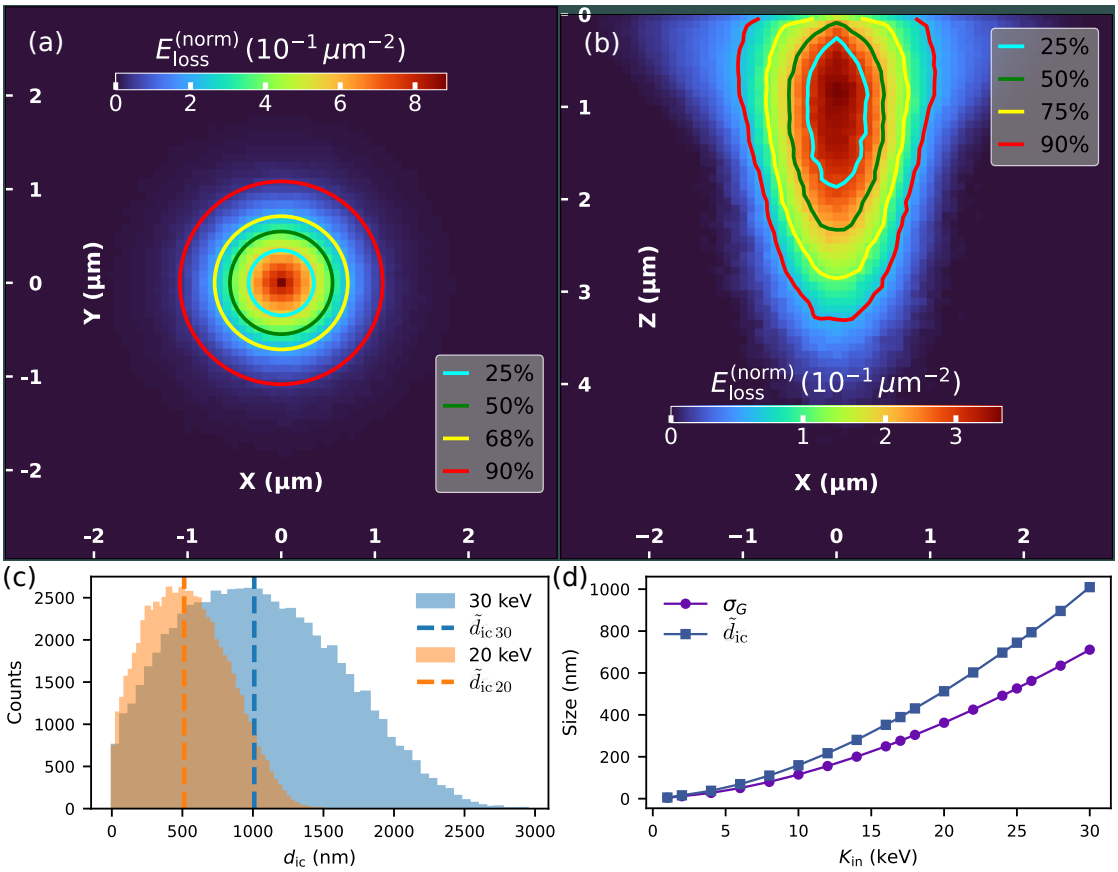

Figure 3.4: Monte Carlo simulation: (a) and (b) normalized xy and xz, respectively, projections of spatial distribution of energy loss by 30 keV incident electrons on the scintillator. Electron trajectories used in the computation are aligned with respect to their coordinates of center of energy loss $r_{\text{coel}} = (x_{\text{coel}}, y_{\text{coel}})$. (c) Histogram of d_{ic} for 30 keV and 20 keV electrons. (d) Radius σ_G (purple dots) of the circle containing 68% of the energy loss and median distance $\tilde{d}_{ic}$ (blue squares) between r_{in} and r_{coel} as a function of the kinetic energy of incident electrons. Reproduced from Ref. [4].

4 Detector Construction

From the Monte Carlo simulations explained in Chapter 3, we find that for electrons incident on the scintillator with kinetic energies in the range $[1, 30]$ keV, the average size of the spatial region of the scintillated light they generate is of the order of 1 µm (see Figure 3.4d). This motivates the idea of constructing a single electron detector with a spatial resolution of the order of 1 µm through the use of an optical system capable of imaging the signals emitted by single electron events. This chapter describes the parts and construction process of such a detector.

The detector consists of two main elements. The first is a scintillator, which forms a vacuum-air interface. When an electron impinges on the scintillator, a portion of its kinetic energy is converted into luminescence emission of photons. The second is an optical system together with a camera used to image the photons emitted due to electrons impinging on the scintillator.

4.1 Scintillator

For this detector, we use a fast Yttrium Aluminum Garnet doped with Cerium (YAG:Ce) scintillator delivered by Crytur ([10]). Its dimensions are 25 mm diameter × 200 µm thin. The scintillator has an index of refraction $n_s = 1.82$ and a decay constant of 70 ns.

In order to optimize the number of detected photons due to incident electrons, the scintillator possesses a 25 nm Al coating on the vacuum-facing surface.

This thickness of the Al coating was chosen by inspection of both

- YAG:Ce-Al interface reflectance as a function of the thickness of the Al coating, and
- kinetic energy loss of electrons when traveling though aluminum.

Using data from Filmetrics® Spectral Reflectance Calculator [23], the YAG:Ce-Al interface reflectance as a function of the thickness of the Al coating is shown in Figure 4.1a below. We find that for a medium of index of refraction $n_s = 1.82$, followed by a 25 nm Al coating, followed by vacuum, the YAG:Ce-Al interface reflectance is $R = 0.836$ at the wavelength of maximum emission of the scintillator $\lambda = 550$ nm.

Recall ([24],[1]) that the collision stopping power of an electron traveling in a material is the average rate of energy loss of the electron per unit of path length, due to Coulomb interactions with the orbital electrons and nucleus of the atoms in the material. And, the radiative stopping power of an electron traveling in a material is the average rate of energy loss of the electron per unit of path length, due to Coulomb interactions with the orbital electrons and nucleus of the atoms in the material in which bremsstrahlung

quanta are emitted. Moreover, the total linear stopping power is the sum of the collision and radiative stopping powers.

The NIST ESTAR Program ([25]) provides, for an electron traveling in aluminum, as a function of its kinetic energy K, its total linear stopping power $S(K)$ (see Figure 4.1b). From this data, for an electron with initial kinetic energy K_0, when entering the aluminum (path length traveled $l(K_0) = 0$), integration of the differential equation

$$S(K) = -\frac{dK}{dl}$$

gives the function

$$K_f \mapsto l(K_f) \coloneqq -\int_{K_0}^{K_f} \frac{dK}{S(K)}.$$

This function is invertible (since $S(K)$ is always positive) and therefore allows getting its inverse function $l \mapsto K_f(l)$ which represents: for an electron such that before entering the aluminum its initial energy is K_0, its final energy when the electron has traveled a path length l in aluminum is $K_f(l)$. The function $K_f(l)$ is plotted in Figure 4.1c for electrons which initially had kinetic energies 30, 25, 20, and 15 keV.

The kinetic energy loss of a 30 keV electron as a function of l is shown in Figure 4.1d. Thus, a 30 keV electron that traveled $l = 50$ nm through aluminum loses 100 eV, which is 0.33 % of its initial energy.

Therefore, for most 30 keV electrons, their energy loss when traveling through the 25 nm Al layer can be considered negligible. The corresponding reflectance for this 25 nm Al thickness according to Figure 4.1a is $R = 0.836$. By decision, the reflectance is not further increased at the expense of increasing the thickness of the Al coating, since this could undesirably increase the spatial extension of the plume of electron trajectories contained in the scintillator region.

4.2 Scintillator holder

The detector is implemented on a modified FEI XL30 Scanning Electon Microscope (SEM). The vacuum inside the chamber can go down to 2.5×10^{-6} mbar. The scintillator forms a window between the SEM specimen chamber (vacuum) and the exterior (atmospheric pressure). In order to allow the scintillator to withstand atmospheric pressure, it is hosted by a CF100 flange (located at the bottom of the SEM chamber) in a configuration described as follows (see Figure 4.2). On the external surface of the flange, it has a blind hole of 26 mm diameter $\times$ 400 µm depth. Inside this hole, it has 13 through holes, each of 4 mm diameter, with the centers of neighboring circles separated by 5 mm, arranged in a honeycomb pattern. Moreover, there are 6 through holes at the outermost positions of the honeycomb pattern of a diameter of only 2 mm (since a wider hole could leave little space for the glue between the scintillator and flange surface). Furthermore, the internal surface of the flange also contains a blind hole of 26 mm diameter $\times$ 1 cm depth, aligned with respect to the external 26 mm diameter blind hole, in order to reduce the length of the 4 mm channels in order to avoid possible blocking of the electron beam when reaching

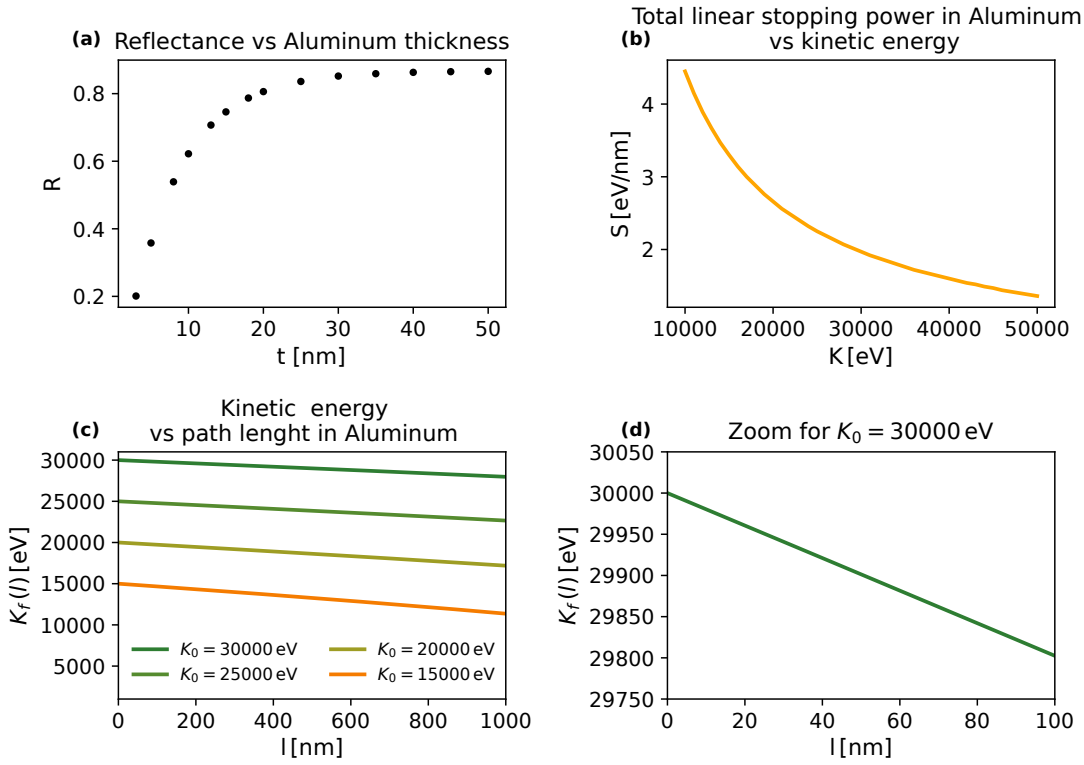

Figure 4.1: (a) Reflectance R at Wavelength of maximum emission of the scintillator ($\lambda = 550\,\text{nm}$) at the YAG:Ce-Al interface as a function of the aluminum layer thickness t. (b) Total linear stopping power S for an electron traveling in aluminum as a function of its kinetic energy K. (c) Kinetic energy K_f of electrons as a function of their path length l in aluminum, for initial kinetic energies of 30, 25, 20, and 15 keV. (d) Zoom to the kinetic energy-traveled distance curve corresponding to the electron with initial kinetic energy $K_0 = 30\,\text{keV}$.

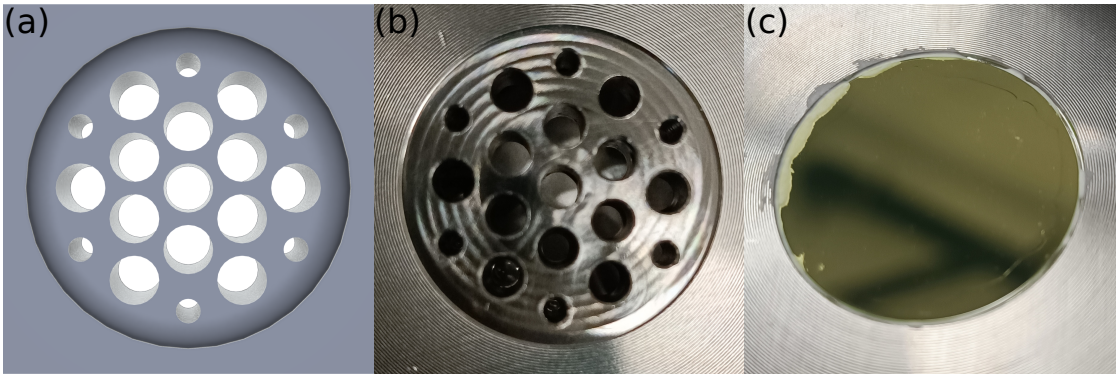

Figure 4.2: (a) 3D model of the holes in the CF100 flange. (b) CF100 flange with the drilled holes. (c) YAG:Ce scintillator glued on the CF100 flange.

a detection region close to the edge of the scintillator. Figure 4.2a shows a 3D model of the holes in the CF100 flange. Along the perimeter of the external 26 mm diameter blind hole, the YAG:Ce scintillator is glued with Torr Seal® Epoxy, with the surface with the Al coating facing inside the SEM. Furthermore, a small drop of conducting paste is placed between the Al surface and the CF100 flange to guarantee a ground connection for the Al surface, and therefore, avoid charging of the Al surface when irradiated by the electron beam. Figure 4.2b shows the external surface of the flange together with the drilled holes, and Figure 4.2c shows the scintillator glued onto the flange as described above.

The choice of a 26 mm diameter $\times$ 400 µm depth blind hole to host the scintillator is made to facilitate insertion of the scintillator when gluing it onto the flange, and to keep the external surface of the scintillator slightly deeper with respect to the external surface of the flange, thus providing some protection for the scintillator surface if the external CF100 surface were to be in contact with another flat surface.

The choice of 4 mm diameter for the holes was made by first performing tests with 18 mm $\times$ 18 mm $\times$ 170 µm microscope cover glasses forming a window between vacuum and atmospheric pressure. The tests were not performed in the SEM vacuum chamber but in other vacuum chambers.

The first test considered circular windows of different diameters, and consisted of finding the maximum diameter of the window before the cover glass would break due to the force difference due to the external atmospheric pressure and the internal low pressure due to the vacuum. These tests were performed on a chamber whose vacuum can go down to ≈ 1 mbar. Notice that the pressure difference across the cover glass is essentially the same for chamber pressures of 1 mbar and 1×10^{-6} mbar, since both are negligible compared to atmospheric pressure (1013.25 mbar). Therefore, the force experienced by the cover glass is approximately the same in both cases. The different circular windows were attained by placing O-rings of different diameters as holders of the cover glass (see Figure 4.3a). It is found that the maximum diameter of the circular window before the 170 µm thick cover glass breaks is of 7.5 mm . Therefore, for the 200 µm thick scintillator, we choose a circular window of 4 mm diameter.

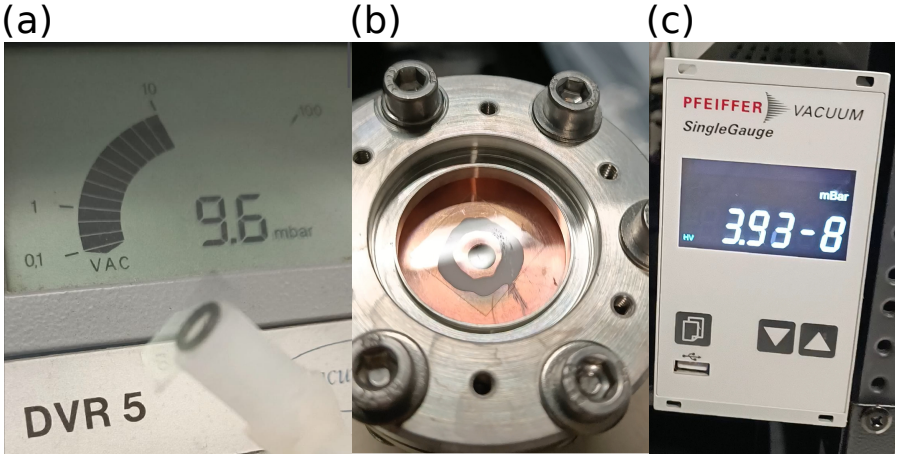

Figure 4.3: (a) 170 µm cover glass forming a vacuum-air interface. In between the cover glass and the tube of the vacuum chamber, there is a 25R6X1.5V75 (7.5 mm central diameter) O-ring to recreate the conditions of a circular window of such dimensions. The vacuum inside the chamber is 9.6 mbar, and the cover glass surface withstands atmospheric pressure. (b) 170 µm cover glass glued on a copper disk with a 5 mm diameter circular through hole in its center, forming a vacuum-air interface. The vacuum inside the chamber is 3.93×10^{-8} mbar as is shown in the pressure gauge reading in figure c.

Furthermore, to test the effectiveness against vacuum leaks by gluing the window with the above described procedure, a test cover glass is glued on a copper disk possessing a 5 mm diameter circular through hole on its center (see Figure 4.3b). The copper disk itself is also used as a gasket to seal the vacuum when installing it in between two CF40 flanges. This test was performed on a chamber whose vacuum can be created by the combination of a Scroll pump, Turbo pump, and Ion pump. Creating a vacuum using the combination of the Scroll pump and Turbo pump (as it is done in the SEM specimen chamber), a pressure of 4.03×10^{-7} mbar is attained. Furthermore, in combination of the Ion pump, a pressure of 3.93×10^{-8} mbar is attained (see Figure 4.3c).

4.3 Optical system and camera

The inside of the scintillator is imaged with an infinity-corrected system. This consists of the high NA=1.40/40X UPlanXApo oil immersion objective from Olympus and a lens, with focal length $f = 50$ mm, AC254-050-A-ML from Thorlabs. The index of refraction of the immersion oil is $n_{oil} = 1.51$. At the focal plane of the 50 mm lens, we place the sensor of the ORCA-Quest qCMOS camera C15550, by Hamamatsu [26]. The camera sensor has a pixel size of 4.6 µm × 4.6 µm and an effective number of pixels of 4096 (H) × 2304 (V). The optical axis is aligned with the center of the camera sensor. Due to space constraints, a 45 deg mirror (PF10-03-P01 from Thorlabs) is mounted in between the objective and the lens, allowing to install the camera perpendicularly to the optical axis

of the objective. The whole detector is isolated from external light sources. A schematic drawing of the setup is shown in Figure 4.4a. Figure 4.4b shows a schematic drawing of an electron trajectory in the YAG:Ce scintillator. Figure 4.4c shows a picture of the detector installed at the bottom of the SEM.

The camera is water-cooled, reaching a sensor temperature of $-34\,^{\circ}\mathrm{C}$, and operated at photon number resolving mode, where the exposure time is $\tau_{\mathrm{exp}} = 0.20\,\mathrm{s}$, and the frame rate is 5 frames/sec.

The choice of using a lens with $f = 50\,\mathrm{mm}$ (instead of the conventional $f = 180\,\mathrm{mm}$ for this Olympus Objective) is to reduce the magnification of the system, thus improving the signal of the detected single electron events. The magnification of this optical system is $\mathrm{M} = 11.40\,\mathrm{X}$, as measured with a micrometer stage.

The focus of the optical system is found by maximizing the peak intensity value of the average point spread function image, which is introduced in Chapter 5.

4.3.1 Collection efficiency of the optical system

Recall that the solid angle Ω of a cone with vertex angle 2θ is given by

$$\Omega(\theta) = 2\pi(1 - \cos(\theta)).$$

In particular, the total solid angle around a point is $4\pi\,\mathrm{sr}$ (4π steradians). Thus, the solid angle Ω of the cone represents the $\frac{\Omega}{4\pi}$ fraction of the total solid angle. This quantity $\frac{\Omega}{4\pi}$ will form part of the calculation of the fraction of emitted photons that are collected by the objective lens, assuming isotropic emission of photons in all directions.

Recall that the photons are emitted from the scintillator medium with index of refraction n_s. A portion of these photons are transmitted to the immersion oil medium with index of refraction n_{oil}, and a portion of these photons are collected by the objective lens. Let θ_{oil} be the maximum collection angle of the objective lens with respect to the optical axis (see Figure 4.5). This angle is given by the numerical aperture of the objective lens $\mathrm{NA} = n_{oil}\sin(\theta_{oil})$. Due to the difference of the index of refraction from the scintillator medium to the oil medium ($n_s > n_{oil}$), the maximum emission angle θ_s of a photon to be collected by the optical system is reduced. By Snell's Law, this angle is given by

$$\theta_s = \arcsin\left(\frac{n_{oil}\sin(\theta_{oil})}{n_s}\right).$$

Thus, the fraction of the emitted photons that are collected by the objective lens, called geometrical collection efficiency, is given by

$$\eta_\Omega = \frac{\Omega(\theta_s)}{4\pi} = \frac{1}{2}(1 - \cos(\theta_s)).$$

Using the identity $\cos(\sin(x)) = \sqrt{1 - x^2}$, one finds that the geometrical collection efficiency is given by

$$\eta_\Omega(n_s, \mathrm{NA}) = \frac{1}{2}\left(1 - \sqrt{1 - \left(\frac{\mathrm{NA}}{n_s}\right)^2}\right).$$

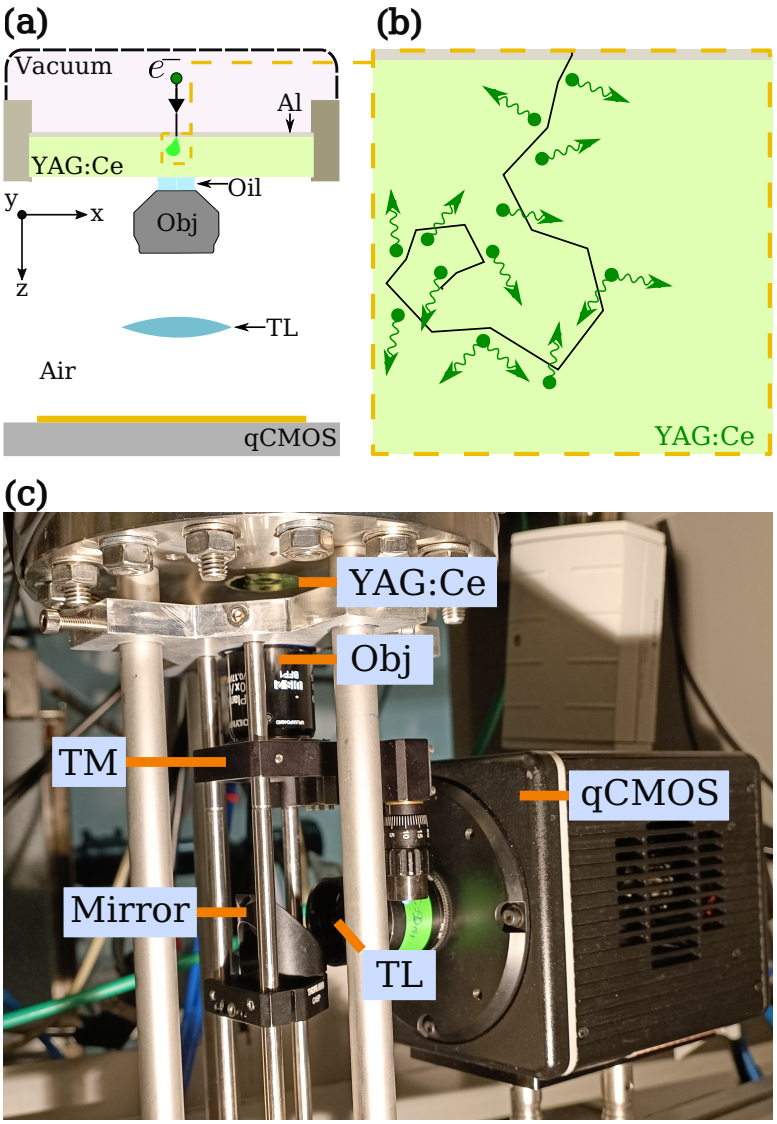

Figure 4.4: (a) Schematic of the setup: an electron e^- impinges into the YAG:Ce scintillator, where a portion of its kinetic energy is converted into luminescence emission of photons. The resulting signal is imaged by an infinity-corrected optical system onto the qCMOS camera sensor. (b) Zoomed-in illustration of the electron trajectory in the YAG:Ce scintillator (black solid line) and the emitted photons (green arrows). (c) Experimental setup: the detector is mounted on a CF100 flange at the bottom of the SEM. At the center of the CF100 flange, the YAG:Ce scintillator window forms the vacuum air interface. The oil immersion objective on a translation mount, together with the mirror and the tube lens, creates the infinity-corrected system that images the electron-induced luminescence onto the qCMOS camera sensor. Reproduced from Ref. [4].

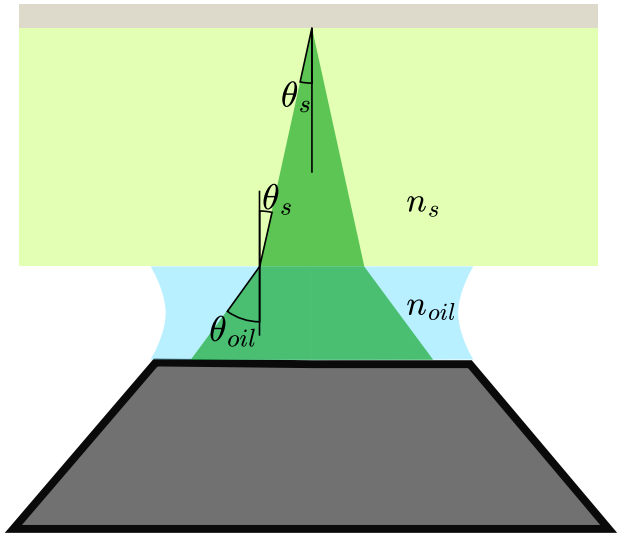

Figure 4.5: Schematic of the maximum emission angle, θ_s, of a photon that can be collected by the optical system. θ_{oil} denotes the maximum collection angle of the objective. n_s and n_{oil} are the indices of refraction of the scintillator and oil mediums, respectively.

Table 4.1 below shows the computed geometrical collection efficiency as a function of different values of refractive index n_s corresponding to different scintillator materials for an oil immersion objective with NA = 1.40.

Scintillator	Refractive index n_s	η_Ω
YAG:Ce	1.82	0.181
GAGG:Ce	1.91	0.160
LYSO:Ce	1.81	0.183
BC-404	1.58	0.268

Table 4.1: Computed geometrical collection efficiency η_Ω as a function of the scintillator refractive index n_s for an oil immersion objective with NA = 1.40. See Section 7.2.4 for additional references on the scintillator characteristics.

In this work the detector operates with a YAG:Ce scintillator, and the corresponding geometrical collection efficiency is $\eta_\Omega = 0.181$. At the wavelength of maximum emission of the scintillator $\lambda = 550\,\text{nm}$ we have the following values. The 25 nm Al coating gives a reflectance $R = 0.836$. The transmission of the objective lens is $\eta_{obj} = 0.90$. The transmission of the tube lens is $\eta_{TL} = 0.98$. The reflectance of the mirror is $R_m = 0.96$.

And the quantum efficiency of the camera is $QE = 0.78$.

Thus, the collection efficiency of the optical system is

$$\eta_{coll} = (1 + R) \cdot \eta_{\Omega} \cdot \eta_{obj} \cdot R_m \cdot \eta_{TL} \cdot QE = 0.22\,.$$

Recall that the light yield of a scintillator, denoted by Y, is the total number of scintillation photons produced per unit of energy deposited by an incident particle.

Let $\overline{\Sigma_{ph}}$ denote the average number of detected photons per incident electron with kinetic energy k_{in}.

Thus $\frac{\overline{\Sigma_{ph}}}{\eta_{coll}}$ is the average number of emitted photons per incident electron with kinetic energy k_{in}. And

$$Y_{eff} = \frac{\overline{\Sigma_{ph}}}{k_{in} \cdot \eta_{coll}}$$

is the average number of emitted photons per unit of incident kinetic energy of an incident electron event. Let

$$\eta_{eff} \coloneqq \frac{Y_{eff}}{Y}.$$

Thus $Y_{eff} = Y \cdot \eta_{eff}$.

η_{eff} is a parameter that accounts for the conversion efficiency of the kinetic energy of an incident electron into the detected photons. In more detail, some factors that the parameter η_{eff} takes into account are:

- Not all incident electrons will deposit all of their kinetic energy since some electrons may be backscattered and leave the material with a non-zero kinetic energy.
- The choice of a high numerical aperture objective ($NA = 1.40$) was to optimize the geometrical collection efficiency η_{Ω} and spatial resolution of the optical system. However, such an increase in the optical resolving power comes accompanied by a reduction of the depth of field (DOF). Thus, an electron whose trajectory extends beyond the DOF may produce scintillation photons in regions that are out of focus. While some of these photons may still be collected, their contribution to a well-localized image may be reduced, lowering the detected photons corresponding to this electron event. Nonetheless, such an electron event may still be detected since a portion of the electron trajectory lies within the DOF, and the scintillated photons within the DOF may still be detected.

For exemplification, consider the case of incident electrons with kinetic energy $k_{in} = 30\,\text{keV}$. As it will be reported in Section 6, we have that $\overline{\Sigma_{ph}} = 26$.

Thus $Y_{eff} = 3.93$ average emitted photons per keV of incident kinetic energy of an incident electron event.

Taking $Y = 30\,\text{photons/keV}$ (as reported by the manufacturer [10]), we get $\eta_{eff} = 0.13\,$. Thus, on average, for a 30 keV incident electron, we detect only 13 % of the photons that would be detected in the ideal case where the electron deposits all its kinetic energy inside the scintillator within a spatial region contained in the DOF of the optical system. One way to increase the value of η_{eff} would be through the use of scintillators with

higher stopping power, as will be described in section 7.2.4, since a higher stopping power reduces the spatial extent of the electron trajectories, thus decreasing the probability that an electron trajectory lies outside the DOF of the optical system.

5 Detection Process

The detection process of an electron, initiated by the impingement of the electron on the scintillator crystal, can be divided into 4 consecutive stages:

1. interactions of the electron with the scintillator, in which a portion of the kinetic energy of the electron is absorbed by the scintillator;

2. the scintillation mechanism, in which a portion of the absorbed energy is converted into luminescence emission of photons;

3. transit of the emitted photons through the optical system to the camera sensor;

4. data processing for detection of events.

Stages 1 and 2 are explained in sections 2.1.1 and 2.1.2, respectively. The optical system and camera are described in section 4.3. In what follows, stage 4 will be explained. Furthermore, it is explained how an estimate of the spatial resolution of the detector is computed with the detected events from stage 4 and with the data derived from the Monte Carlo Simulations explained in Chapter 3.

5.1 Data processing for detection of events and computation of spatial resolution estimate of the detector

In what follows, the data processing for detection of electron events and the computation of an estimate of the spatial resolution of the detector are explained. For example, the case of 30 keV electrons is discussed. Spatial parameters in the analysis are worked in terms of pixels. The conversion factor from number of pixels to size at the scintillator is $\texttt{pix\_to\_dist} = 4.6\,\mu\text{m}/11.4\,\text{px} = 0.40\,\mu\text{m/px}$, where $M = 11.4$ is the magnification of the optical system.

Suppose that, during a time interval, electrons have impinged into the scintillator and their signals have been captured in a series of frames. These frames are analyzed in Python for detection of these signals. When the electron source is blocked, a series of frames of the ambient background is also taken.

Data processing for detection of events

The data processing algorithm can be divided into the following steps.

1. Cropping region of interest

For both, frames with single electron signals and frames of ambient background, the region of interest (ROI) to analyze consists of a circle of diameter $D_{\mathrm{ROI}} = 2 \cdot r + 1\,\mathrm{px} = 801\,\mathrm{px} = 320.4\,\mu\mathrm{m}$ with its center coinciding with the center of the full frame, where $r = 400\,\mathrm{px}$ is the radius of the ROI. Each frame is cropped to a square with sides of dimension $2 \cdot (r + r_{\mathrm{m}}) + 1\,\mathrm{px}$ concentric with the circle defining the ROI. In the previous expression, $r_{\mathrm{m}} = 22\,\mathrm{px}$ is a margin to allow future cropping of areas around events close to the edge of the FOV.

Average background image and dead pixels

Taking the average along the background frames gives the average background image, which is used for background subtraction. Similarly, taking the standard deviation, pixel-wise, along the background frames gives the standard deviation of the background image. Next, we define a set of dead pixels, which consists of all the pixels that lie above the 99.99 th percentile of both the histogram of the average background image and the histogram of the standard deviation of the background image. A detected event close to a dead pixel will be rejected, as will be explained below in step 5.

2. Background subtraction and Gaussian Filter

First, from each frame to be analyzed (`frame_raw`), the average background image is subtracted. Then, a normalized Gaussian filter of circular kernel is applied, thus obtaining the image `frame_filtered`. The value of sigma σ_G defining the Gaussian function of the applied Gaussian filter is taken to be half of the diameter of the circle from where 68 % of the scintillated photons are emitted, which was calculated with the Monte Carlo simulation (see Figure 3.4d). For 30keV, $\sigma_G = 1.762\,\mathrm{px} = 0.705\,\mu\mathrm{m}$. The diameter of the circular kernel is $2 \cdot (\mathrm{round}(2\sigma_G)) + 1\,\mathrm{px}$. The filtered frames are used to identify the location of electron signals.

The filtered frames represent a correlation map between the signals in the `frame_raw` and the PSF modeled by the Gaussian filter kernel. Thus, the local maxima in the filtered frames correspond to the locations of highest correlation and are therefore used as the coordinates of candidate electron events.

3. Local maxima identification

For each filtered frame, `frame_filtered`, the coordinates of its local maxima are calculated. These are calculated with the function `peak_local_max` from the `scikit-image` Python library [27], which internally uses a maximum filter for finding the local maxima. The positions of the found local maxima are taken as the coordinates of the detected events. Each of them can either correspond to a local maximum artificially generated by noise or generated by a legitimate electron signal. If a local maxima corresponds to an electron signal (according to the classification described in step 7), then the coordinates of this

local maxima are taken as the coordinates of the center of energy loss of the electron signal.

4. Detected photons calculation

The total number of detected photons, denoted Σ_{ph}, for the event with coordinates (i, j) is the sum of all photons detected within, including the border, a circle of diameter $d_{\text{ref}} = 13\,\text{px} = 5.2\,\mu\text{m}$ centered at the pixel (i, j). As will be explained below, the events will be characterized by their Σ_{ph}, and this parameter will be used to define the classification between noise events and electron events. This choice of d_{ref} optimizes the discrimination of electron events from noise events.

It can happen that close to the neighborhood of the signal of a legitimate electron, there is a weak local maxima corresponding to noise. Thus, when computing the Σ_{ph} for this noise event, this might get contributions to its Σ_{ph}, coming from the signal of a legitimate electron. This is not desirable since the noise event is being attributed a signal that does not correspond to itself, thus affecting the Σ_{ph} histogram analysis and binary classification to be explained below. To resolve this problem, when detecting the coordinates of local maxima, if the distance between two detected local maxima is smaller than d_{ref}, then the local maxima with smaller intensity is rejected. Furthermore, the electron beam current is reduced so that the density of electron events is low, increasing the probability of isolated electron signals, which is desirable for an accurate characterization of the total number of detected photons in single-electron events.

5. Filtering spurious events and events close to dead pixels

Defects in the silicon wafer of the CMOS image sensor may cause high-dark-current pixels [28]. These pixels appear brighter than the surrounding pixels, and are called white spots or hot pixels.

After applying the Gaussian filter to a region around a hot pixel, the filtered frame in that region may resemble the signal produced by an electron event. Consequently, hot pixels may generate undesired entries, called spurious events, in the list of detected local-maxima events. These spurious events are therefore rejected as described below.

By inspection of many single electron signals, we notice that a value equal to or greater than 7 counts for a single pixel is not common. The spurious events appear as single bright pixels with count values equal to or greater than 7 counts, with immediate neighbor pixels with low counts (0 counts or 1 count). For each detected event, it is calculated the difference of the maximum and minimum pixel value in an area corresponding to a square window of dimension $2 \cdot 6 + 1\,\text{px}$ centered at the event coordinates. If this difference is higher than a threshold $T_{\text{spurious}} = 7$, then the corresponding event is rejected.

Furthermore, a filter accounting for dead pixels (defined in step 1) is also applied. A detected event whose coordinates are closer than $D_{\text{dead pixel}} = 6\,\text{px}$ to a dead pixel is rejected.

We now have a list of detected events of local maxima with their corresponding coordinates, frame number, and Σ_{ph} value. For this list of events, consider the histogram

of their Σ_{ph} values.

Noise Model

Performing the above procedure on the data set of ambient background images, the obtained histogram, describing the noise, is shown in Figure 5.1a. This histogram (orange dots) is found to obey a log-normal distribution. We thus obtain that, for this analysis, the model of the noise is given by a log-normal distribution, i.e. the histogram of Σ_{ph} of events of local maxima of noise follows a log-normal distribution.

Furthermore, this is confirmed by simulating a data set of ambient background images with underlying Poissonian statistics, using the specifications of the camera, and applying to it the above-mentioned procedure. The obtained histogram is shown in Figure 5.1b, verifying that the histogram of Σ_{ph} of events of local maxima of noise follows a log-normal distribution.

Recall that if $X_1, \ldots, X_n$ ($n \in \mathbb{N}_+$) are independent random variables, and for each $i \in \{1, \ldots n\}$, X_i obeys a Poisson distribution with mean λ_i, then $Y \coloneqq \Sigma_{i=1}^{n} X_i$ obeys a Poisson distribution with mean $\Sigma_{i=1}^{n} \lambda_i$ [29]. Now it will be explained why the histogram of Σ_{ph} (sum of values of Poisson distributions) does not obey a Poisson distribution. This is because the histogram of Σ_{ph} (sum of values of Poisson distributions) includes only those sums centered at the location of local maxima, and this introduces a bias, which leads to a distribution that is Log-Normal, rather than Poissonian. This is further confirmed with the simulated data set of ambient background images. If one does not consider only the local maxima coordinates, but all pixels, then the obtained histogram of Σ_{ph} obeys a Poisson distribution, as expected (see Figure 5.2b). If one considers only the local maxima coordinates, then the obtained histogram of Σ_{ph} does not obey a Poisson distribution, but rather a Log-Normal distribution (see Figure 5.2a).

6. Σ_{ph} histogram and distribution fitting

Performing the above procedure to the data set with single electron signals, one obtains the histogram of values of Σ_{ph} of events of local maxima (see Figure 6.1d). To this histogram, a function of the form

$$C_l \cdot \text{log\_normal\_distribution} + C_n \cdot \text{normal\_distribution} \tag{5.1}$$

is fitted. The log-normal distribution and normal distribution represent, respectively, the events of local maxima artificially generated by noise, and the events of local maxima of electron signals.

7. Binary classification

We use this histogram for performing a binary classification on our set of detected events. For this, a minimum threshold, T_{rm}, of Σ_{ph} is chosen. An event with $\Sigma_{ph} \geq T_{\text{rm}}$ is classified as positive, i.e. considered as an electron event, and an event with $\Sigma_{ph} < T_{\text{rm}}$

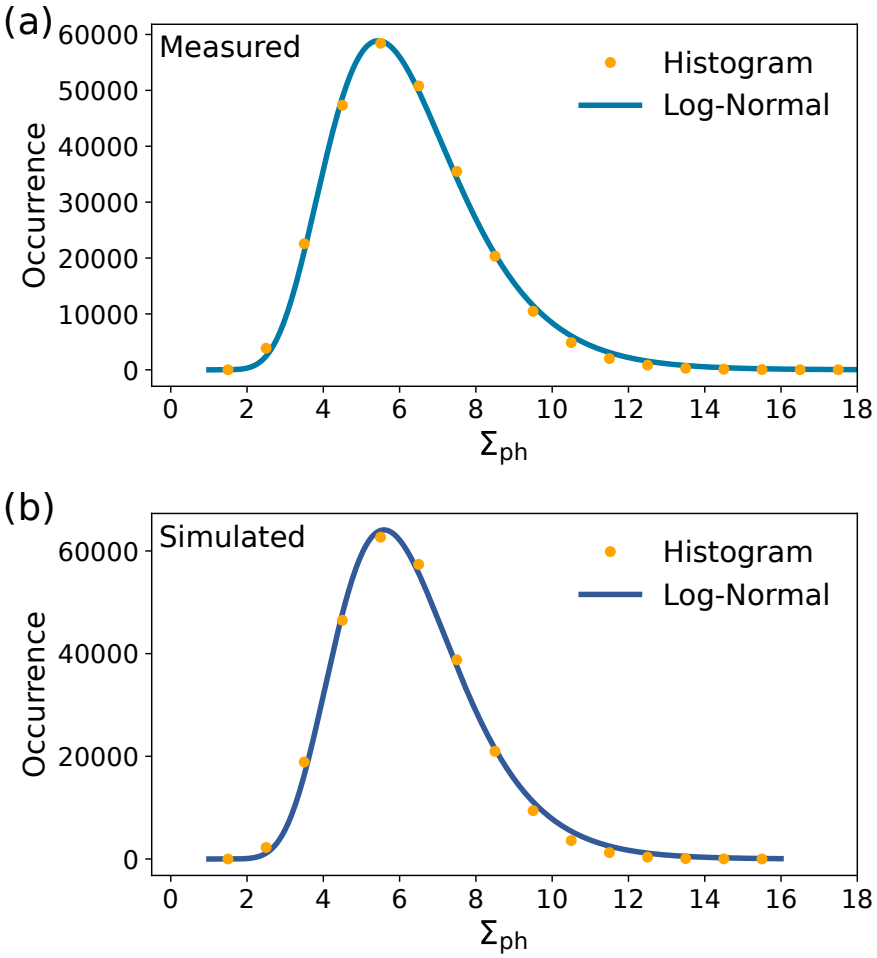

Figure 5.1: Background photon number distribution: (a) experimental histogram (orange dots) of values of Σ_{ph} photons contained in circle of diameter $d_{\text{ref}} = 13\,\text{px}$ centered at local maxima coordinates of gaussian filtered images of dark background, and Log-Normal fit of the distribution. (b) simulated histogram using the specifications of the camera. Reproduced from the supporting information of Ref. [4].

is classified as negative, i.e. considered as a noise event. The true positives (TP), false positives (FP), true negatives (TN), and false negatives (FN) are given by

$$TP \coloneqq \int_{T_{\text{rm}}}^{\infty} N(x)dx \quad FP \coloneqq \int_{0}^{T_{\text{rm}}} N(x)dx$$

$$TN \coloneqq \int_{0}^{T_{\text{rm}}} L_{\text{N}}(x)dx \quad FN \coloneqq \int_{T_{\text{rm}}}^{\infty} L_{\text{N}}(x)dx$$

where N and L_{N} are, respectively, the fitted normal and log-normal distributions.

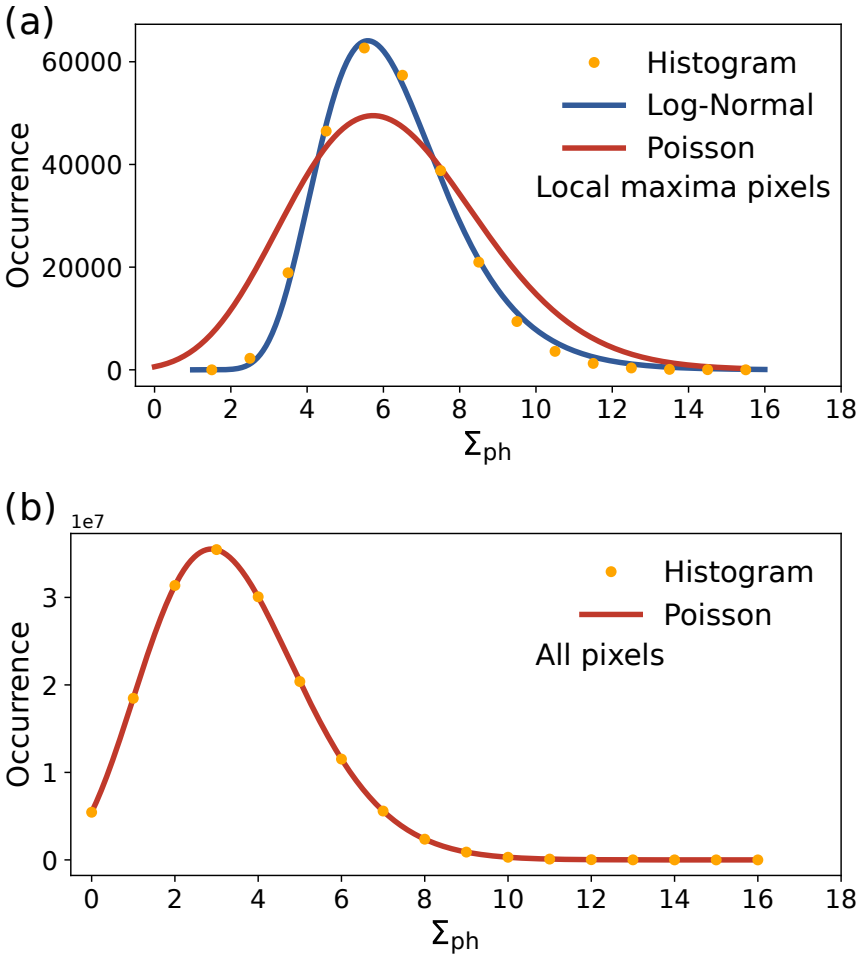

Figure 5.2: Simulated background photon number distributions: (a) histogram (orange dots) of values of Σ_{ph} at coordinates of local maxima and Log-Normal and Poisson fits of the distribution. (b) histogram (orange dots) of values of Σ_{ph} at coordinates of all pixels and Poisson fit of the distribution. Adapted from Ref. [4].

These four numbers define the confusion matrix of the binary classification, which is shown in Figure 6.1d.

Performance of the binary classification

The performance of the binary classification for a particular choice of threshold T_{rm} is described jointly by the efficiency, $\eta := \frac{\mathrm{TP}}{\mathrm{TP+FN}}$, which describes the fraction of all actual electron events that are classified as electrons, and purity, $p := \frac{\mathrm{TP}}{\mathrm{TP+FP}}$, which describes the fraction of all electron-classified events that are actually electron events.

The performance is also be described by the F_1-score, $F_1 \coloneqq 2 \cdot \frac{\eta \cdot \mathrm{p}}{\eta + \mathrm{p}}$. The set of points $\{(T_{\mathrm{rm}}, \eta(T_{\mathrm{rm}}), p(T_{\mathrm{rm}}) : T_{\mathrm{rm}} \in \mathbb{N}\}$ defines the efficiency-purity curve in the $\eta - p$ plane, and it describes the performance of the binary classification for arbitrary choices of threshold. The maximum F_1-score attained at a point $(\eta(T_{\mathrm{rm-max}}), p(T_{\mathrm{rm-max}})$ along the curve, defines the threshold $T_{\mathrm{rm-max}}$ which represents an optimal compromise that can be achieved between efficiency and purity. Notice that depending on the application, one may choose a different threshold that may prioritize one parameter (η or p) over the other. All of these metrics are computed with the information of the fitted function 5.1.

Up to now, the data processing for the detection of single electron events has been explained. Next, the computation of the spatial resolution estimate of the detector using the data from detected single electron events will be described.

Computation of spatial resolution estimate of the detector

The spatial resolution estimate for single electron detection is determined by two factors:

1. The average size of the imaged electron signals, described by the FWHM of the average point spread function (PSF) image obtained by averaging across many electron signals. This FWHM gives a criterion of the closest distance at which two imaged electron signals can be discriminated.

   Notice that the coordinates of a detected light signal due to an electron are taken as the coordinates of center of energy loss of the electron event. This is, the position of the detected light signal does not correspond to the position of incidence of the electron at the scintillator but rather to its coordinates of center of energy loss. This displacement due to the random walk of the electron in the scintillator is taken into account by considering:

2. the median $\tilde{d}_{ic}$ of the distances d_{ic} between the transversal coordinates of incidence r_{in} and of center of energy loss r_{coel}.

The computation of the FWHM of the average PSF is explained below in steps 8 and 9. The value of $\tilde{d}_{ic}$, was computed with the Monte Carlo Simulations as a function of the kinetic energy of the incident electrons in Chapter 3 (see Figure 3.4d).

Thus, the spatial resolution estimate of the detector is given by

$$\delta x \coloneqq \sqrt{\mathrm{FWHM}^2 + (2\tilde{d}_{ic})^2}.$$

This δx is a conservative criterion of a spatial distance such that if the distance between the positions of two electron signals is not smaller than δx, then it is likely that the incidence positions of the electrons at the scintillator occurred at spatially distinct regions. For a detailed discussion regarding the spatial resolution of the detector, see the criteria of spatial resolution in section 5.2.

8. Computation of average PSF image

The average PSF image is computed by superposing many electron signals. For the calculation of this average PSF image of electron signals, we choose the threshold $T_{\mathrm{rm}} = 17\,\mathrm{photons}$. The corresponding performance of the binary classification is $(\eta, p) = (0.92, 0.99)$. This choice is made to have a high certainty that all the considered events do correspond to actual electrons. For the computation of the average PSF image, 89275 electron events were used.

The average PSF image is computed as follows. Consider the set of detected electron events, i.e. the set of events classified as positive. For each detected event, a square region of odd size $2 \cdot d_{\mathrm{region\_plot}} + 1\,\mathrm{px} = 2 \cdot 12 + 1\,\mathrm{px} = 25\,\mathrm{px}$ centered at the coordinate of the event, is cropped. One thus obtains a series of images, each containing the signal of a detected electron, with the coordinate of the signal coinciding at the same pixel at the center of the image. The average along these images is computed. The average image thus obtained is the average PSF image.

9. Computation of FWHM of the average PSF image

The computation of the FWHM of the average PSF image is now explained. First, the average background is computed as the average across all pixels of the average background image. With respect to the background height, the half maximum of the average PSF image is computed. Consider the profile along the horizontal axis passing through the center of the image (Figure 6.1d shows this profile as a green line). By linear interpolation, one finds the two horizontal coordinates at which the profile achieves the half maximum. The distance between these horizontal coordinates is the $\mathrm{FWHM_x}$. Similarly, considering the profile along the vertical axis passing though the center of the image, one computes the $\mathrm{FWHM_y}$. The FWHM of the average PSF is given by the average of the above computed values of FWHM for each profile, i.e. $\mathrm{FWHM} = \frac{\mathrm{FWHM_x} + \mathrm{FWHM_y}}{2}$.

Analysis for kinetic energies in the range [17 keV, 30 keV]

The above described procedure is repeated for the energies in the range of $[17\,\mathrm{keV}, 30\,\mathrm{keV}]$. As explained in step 2, for each value of kinetic energy, the value of sigma (σ_g) defining the Gaussian function of the applied Gaussian filter is taken to be half of the diameter of the circle from where 68 % of the scintillated photons are emitted, which was calculated with the Monte Carlo simulation (see Figure 3.4d). Moreover, the spatial resolution estimate of the detector is computed using the value of $\tilde{d}_{ic}$ corresponding to the kinetic energy of the incident electrons (see Figure 3.4d).

5.2 Criteria of spatial resolution

The fact that in general there is a non-zero displacement between the position of incidence r_{in} and the position of detection r_{det} of an electron event, introduces an uncertainty δd for the determination of the position of incidence r_{in} of the electron at the detector. This

leads us to rethink the criterion of spatial resolution of the detector. In what follows, it will be explained different criteria of spatial resolution that can be taken into account. Notice the difference between the positions of the detected electron signals and the positions of incidence of the electrons at the scintillator. Also note that, once the detection position of an electron r_{det} has been determined, we know that for $n\,\%$ of the electron events the corresponding position of incidence r_{in} lies within a circle of radius δd centered at r_{det}. Here, δd is defined as the n-th percentile of the distances d_{id} between the incidence position of the electron event r_{in} and the detection position r_{det}. In what follows, the spatial region of this circle will be called the predicted region of incidence of the electron event.

C1 The closest distance between the positions of two electron signals at which one can distinguish the two electron signals is the FWHM of the average electron signal.

Notice that even if the positions of incidence of two electron events are separated by a distance of $2 \cdot \delta d$, their corresponding positions of detection could be closer than the distance of the FWHM and one would therefore have no guarantee that one will be able to distinguish that there did happen two electron events. We thus need a criterion that guarantees us that if two electrons incide on the scintillator, we will be able to distinguish that two electron events were detected.

C2 The closest distance between the positions of incidence of two electron signals at which one is guaranteed (for $n\,\%$ of the electron events) to be able to distinguish their corresponding electron signals is FWHM $+ 2 \cdot \delta d$.

Notice that even if one is guaranteed to distinguish two electron signals, their corresponding predicted regions of incidence may share an area in common. This implies that there is also some degree of uncertainty on whether or not the two electron events incided at the same position of the scintillator or not. The less area in common between the predicted regions of incidence, the less probable that both electron events incided at the same position at the scintillator.

C3 Suppose that the FWHM is smaller than $2 \cdot \delta d$. The closest distance between the positions of two electron signals at which (for $n\,\%$ of the electron events) the measured regions of incidence of the two electron events do not possess area in common is $2 \cdot \delta d$. That is, the incidence positions of the electrons at the scintillator occurred at spatially distinct regions.

C4 Notice that for smaller values of kinetic energy k_{in}, it could happen that δd becomes smaller than the FWHM. This happens when K_{in} is small so that δd is much smaller than the resolution limit of the optical system. One could also have a scintillator of such high total stopping power that δd is much smaller than the resolution limit of the optical system, and thus δd is smaller than the measured FWHM. One therefore needs a criterion of spatial resolution that is valid in all these possible cases, so that one is able to do a meaningful comparison of the spatial resolution across different ranges of k_{in} of the incident electrons and across different scintillator materials. A

criterion fulfilling this purpose is given by the quantity $\delta x \coloneqq \sqrt{\mathrm{FWHM}^2 + (2 \cdot \delta d)^2}$. Notice that in the limit when $\delta d \ll \mathrm{FWHM}$ one recovers the criterion C1. And in the limit when $\delta d \gg \mathrm{FWHM}$ one recovers the criterion C3. Thus δx is a conservative criterion of a spatial distance such that if the distance between the positions of two electron signals is not smaller than δx, then (for $n\,\%$ of the electron events) the measured regions of incidence of the two electron events will not possess area in common. That is, the incidence positions of the electrons at the scintillator occurred at spatially distinct regions.

C5 Suppose that the FWHM is smaller than $4 \cdot \delta d$. The closest distance between the positions of incidence of two electron signals at which one is guaranteed (for $n\,\%$ of the electron events) that their corresponding predicted regions of incidence will possess no area in common, is $4 \cdot \delta d$.

6 Results — Detector Characteristics

6.1 Detection of single electrons with kinetic energy of 30 keV

The results of the detection process of 30 keV electrons, explained in detail in section 5.1, are now presented. Figure 6.1a shows a square subregion of a raw data frame containing electron signals. Figure 6.1b shows the same subregion after subtracting the average background image and applying the Gaussian filter. The histogram of values of Σ_{ph} of events of local maxima is shown in Figure 6.1d together with a fit of it with a function of the form 5.1. The fitted normal distribution possesses a mean photon number of $\overline{\Sigma_{ph}} = 26$ and a standard deviation of $\sigma_n = 6.4$ photons.

The efficiency-purity curve describing the different performances that can be achieved by the binary classifications defined by the choice of a threshold T_{rm} is shown in Figure 6.1c. In particular, it is indicated with a red dot the efficiency and purity values $(\eta, p) = (0.96, 0.96)$ corresponding to the best F_1-score $F_1 = 0.96$ attained with a binary classification defined by the threshold $T_{\mathrm{rm}} = 15$ photons.

For the calculation of the average PSF image of electron signals, a threshold of $T_{\mathrm{rm}} = 17$ (vertical dashed line in Figure 6.1d) photons is used, resulting in a purity of the electron-classified events of $p = 0.99$. The confusion matrix describing the binary classification defined by this choice of threshold is shown in Figure 6.1d. The average PSF image is computed by averaging over 89275 electron-classified events. The PSF cross-section is shown in Figure 6.1d (S, green line), together with the average background (B, blue line). The FWHM of the PSF is FWHM$= 1.04\,\mu$m. The median of the distances d_{ic} is $\tilde{d}_{ic} = 1009\,$nm. Thus, the spatial resolution estimate of the detector for single 30 keV electrons is $\delta x \coloneqq \sqrt{\mathrm{FWHM}^2 + (2\tilde{d}_{ic})^2} = 2.3\,\mu$m.

6.2 Detection of single electrons with kinetic energy in the range [17 keV, 30 keV]

The detector characteristics as a function of the kinetic energy of the electrons is now presented. Figure 6.2a shows the measured FWHM as a function of the kinetic energy K_{in} of the incident electrons. Notice that this increases with K_{in}, as expected, since the energy deposited by the incident electron can potentially be spread in a wider area. For energies below 20 keV the curve flattens, mainly as a consequence of the effective pixel size at the scintillator plane ($0.4\,\mu$m). For 17 keV electrons, the FWHM of the PSF is FWHM$= 0.51\,\mu$m. The median of the distances d_{ic} is $\tilde{d}_{ic} = 390\,$nm. Thus, the spatial

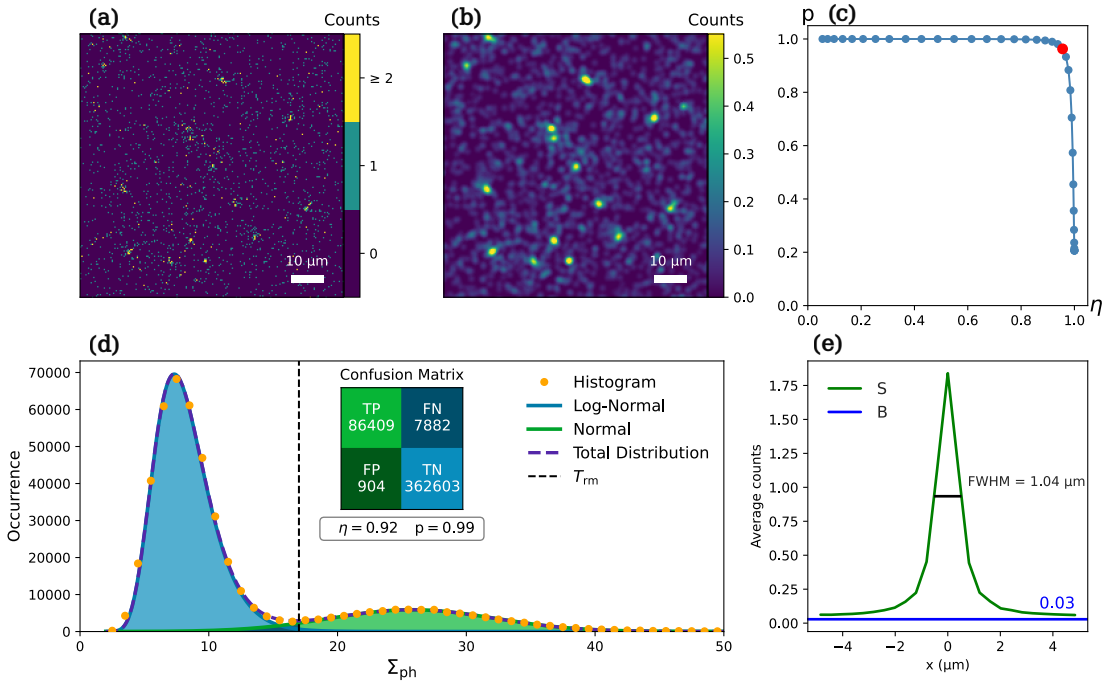

Figure 6.1: Data analysis for 30 keV electrons: (a) Zoom-in of a square subregion of the raw data frame; (b) Same subregion after background subtraction and application of the Gaussian filter. (c) efficiency η versus purity p curve, with the maximum F_1-score indicated as a red dot. (d) Histogram (orange dots) of photon counts within a circle of diameter d_{ref}, centered at local maxima of the Gaussian-filtered image. The histogram is fit with a linear combination of Log-Normal and Normal distributions. The confusion matrix presented in the figure is calculated with a threshold $T_{\text{rm}} = 17$ counts, which optimizes the purity to $p = 0.99$, and it represents the binary classification used to select events for computing the average PSF. (e) Cross section of the average PSF (S, green line) with corresponding FWHM = 1.04 μm, and the average background (B, blue line). Reproduced from Ref. [4].

resolution estimate of the detector for single 17 keV electrons is $\delta x = 0.9\,\mu$m.

Figure 6.2b shows the mean photon counts T_{rm} per detected event as a function of K_{in}. This data is fitted with a linear regression, obtaining a slope of 0.67 average detected photons per keV, and intercept of 4.8 photons. Notice that this intercept of 4.8 photons is in good agreement with the measured $\overline{\Sigma_{ph}}$ of the background (see Figure 5.1a). For 17 keV electrons we have a mean number of detected photons of $\overline{\Sigma_{ph}} = 16.6$.

Figure 6.2c shows, for each value of K_{in} of the incident electrons, the corresponding efficiency-purity curve describing the different performance that can be achieved by the binary classifications defined by each choice of a threshold T_{rm}. Notice that the closer the curve is to the point of the ideal binary classification performance $(\eta, p) = (1, 1)$, the better

the binary classification performances that can be achieved along the segment of the curve that is close to this point. Notice that the higher the energy of the incident electrons, the better are the performances of the binary classifications that can be achieved, as expected, given that higher energy electrons produce higher intensity signals, which makes their discrimination from the background easier.

Finally, the best F_1-score for each value of K_{in}, is shown in Figure 6.2d, together with its respective efficiency and purity. Notice that for $K_{in} = 17\,\text{keV}$, one has $F_1 = 0.8$ and it increases with K_{in} reaching $F_1 = 0.96$ at $K_{in} = 30\,\text{keV}$.

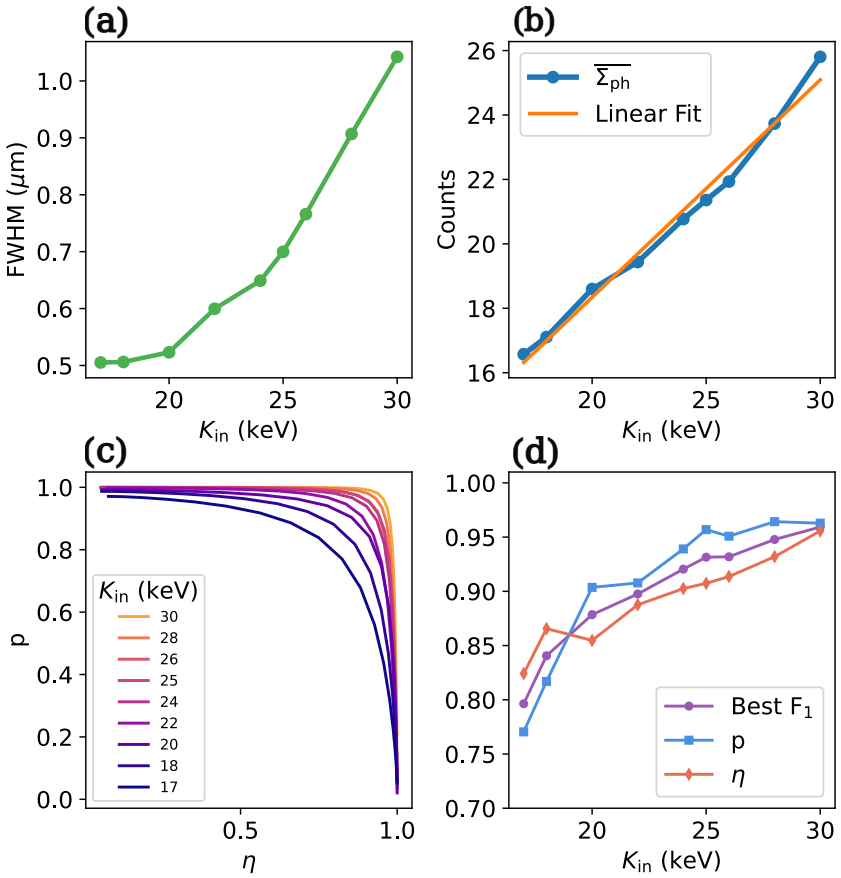

Figure 6.2: (a) Measured FWHM of the average PSF as a function of energy. (b) Mean photon counts per detected event as a function of energy (blue line, round markers) and linear fit (orange line). The linear fit has a slope of 0.67 photons/keV and an intercept of 4.8 photons. (c) efficiency-purity curves for electron energies between 17 keV and 30 keV. (d) Best F_1-score and corresponding purity p and efficiency η values as a function of electron energy. Reproduced from Ref. [4].

Figure 6.3 shows the spatial resolution estimate δx as a function of the kinetic energy K_{in} of the incident electrons. For 20 keV electrons, $\delta x(20\,\text{keV}) = 1.2\,\mu\text{m}$, and for 18 keV

electrons, $\delta x(18\,\mathrm{keV}) = 1.0\,\mu\mathrm{m}$. Hence, for electron energies below 18 keV, the spatial resolution estimate for single-electron detection is below 1 µm.

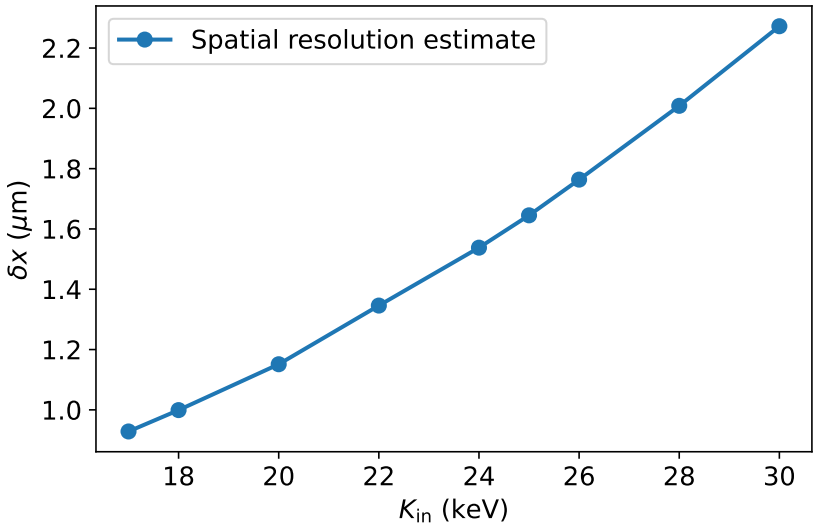

Figure 6.3: Spatial resolution estimate as a function of energy. Based on Ref. [4].

7 Conclusions and Future Work

7.1 Conclusions

We have experimentally demonstrated single-electron detection with an estimated energy-dependent spatial resolution of the order of 1 µm. At an electron energy of 17 keV, the spatial resolution estimate is $\delta x = 0.9\,\mu\text{m}$; and at an electron energy of 30 keV, the spatial resolution estimate is $\delta x = 2.3\,\mu\text{m}$. For electron energies below 18 keV, the spatial resolution estimate for single-electron detection is below 1 µm.

The detector is able to discriminate single-electron events from the background noise with high efficiency and purity. For 30 keV electrons, the best F_1-score is $F_1 = 0.96$ with corresponding efficiency and purity of $(\eta, p) = (0.96, 0.96)$; and for 17 keV electrons, the best F_1-score is $F_1 = 0.80$ with corresponding efficiency and purity of $(\eta, p) = (0.82, 0.77)$

Furthermore, the detector is able to measure the number of detected photons per each electron event, yielding a mean number of detected photons of $\overline{\Sigma_{ph}} = 16.6$ for 17 keV electrons and of $\overline{\Sigma_{ph}} = 26$ photons for 30 keV electrons.

The spatial resolution of this detector is approximately 5× higher than that of state-of-the-art direct electron detectors. For instance, compare it with monolithic active pixel sensors, which offer pixel sizes down to 5 µm [8, 9], or with hybrid pixel array detectors, which offer pixel sizes of $55 \times 55\,\mu\text{m}$ [6] or larger [7].

The high spatial resolution of this detector enables electron diffraction studies at sub-millimeter distances between the sample and the detection screen, as it is demonstrated in [4]. Furthermore, it will enable more sensitive quantum electron optics experiments, such as ponderomotive wavefront shaping in a low-intensity limit [11, 12].

7.2 Future Work

7.2.1 Direct measurement of the energy-dependent spatial resolution for single-electron detection

Notice that the measured position of detection r_{det} of an electron event, given by a specified data analysis scheme, in general will not coincide with the position of incidence r_{in} of the electron at the scintillator, which is the actual coordinate of detection of interest. This introduces an uncertainty δd for the determination of the position of incidence r_{in} of the electron at the detector. At each specified kinetic energy of incidence of the electrons k_{in}, this uncertainty δd, together with the FWHM of the average electron signal, will play an important role in describing the spatial resolution of the detector. In what follows, it will be discussed how this uncertainty δd may be defined and experimentally measured.

In order to do a measurement of δd, we need to experimentally measure, for many single-electron events, the distance d_{id} between the position of incidence of the electron event r_{in} and the position of detection r_{det} of the electron event, given by the data analysis scheme that happens to be employed. From the obtained data set of these measurements, one may define δd as the n th percentile of the measured distances (90 thpercentile, for example). Hence, when discussing the spatial resolution criterion of the detector, this will be true for n % of the detected electron signals (90 % of the detected electron signals, for example).

For each single-electron event, one therefore needs two measurements, namely the position of incidence r_{in} and the position of detection r_{det}. The position of detection will be given by the employed data analysis scheme. The position of incidence r_{in} may be measured as follows.

First, one needs to focus a continuous electron beam with a width much smaller than the spatial resolution we intend to measure. For instance, we know that the spatial resolution is of the order of 1 µm, so in what follows suppose that we focus the electron beam to a width of the order of 1 nm at the scintillator incidence surface. The fact that now many electrons will arrive at the exact same position (with an uncertainty of the order of 1 nm) will increase the overall energy deposition at the position of incidence, yielding a noticeable peak of intensity of the emitted photons at that location. Figures 7.1a and b show the normalized xy and xz, respectively, projections of the spatial distribution of absorbed energy due to a 1 nm in diameter 30 keV electron beam incident on the scintillator. There one can notice the high-intensity peak in the energy absorbed by the scintillator due to the arrival of many electrons on the same circular area of 1 nm in diameter. The simulations were performed with the CASINO simulation software [13].

The spatial resolution of the detector in this continuous mode is improved by the fact that now there is no unknown position of incidence, since now the maximum of the detected signal corresponds to the position of incidence of the beam. The signal of the beam can then, for instance, be fitted with a Gaussian function, where the position of its maxima defines the position of incidence of the beam. Moreover, multiple measurements of this position allow us to determine the position of incidence of the electron beam with high precision. Once the position of incidence of the electron beam has been determined with good precision, one can reduce the beam current until achieving a single-electron event per frame. For these single-electron events we can therefore compute their positions of detection d_{det}, with the specified data analysis scheme, and it is already known that the positions of incidence of all of these single-electron events are given by the previously measured position of incidence of the electron beam.

In this work the FWHM was measured experimentally. However, the uncertainty δd was not measured experimentally but rather was computed with a Monte Carlo Simulation. In the simulation, it was assumed that the position of detection of our data analysis scheme was described by the position of center of energy loss r_{coel} of the simulation. One then computed the distance d_{ic} between the simulated position of incidence r_{in} and position of center of energy loss r_{coel}. And repeating this calculation for many electron energies, we used the median of all distances $\tilde{d}_{ic}$ as the uncertainty δd. This is, we took $\delta d = \tilde{d}_{ic}$.

The uncertainty δd was not measured experimentally due to the limitation of achieving

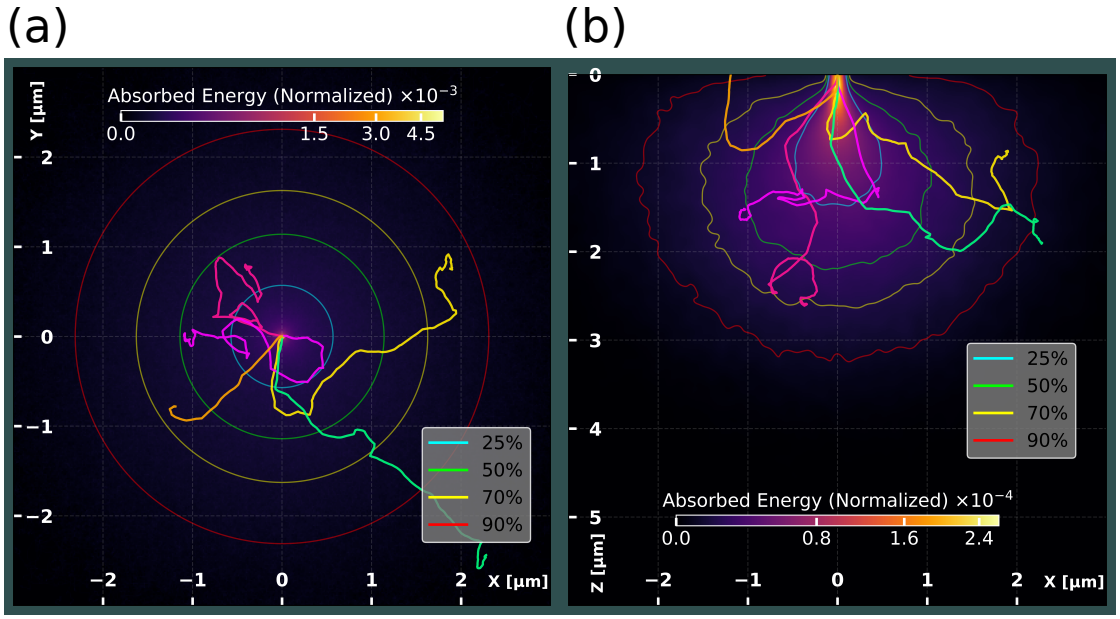

Figure 7.1: Monte Carlo simulation: (a) and (b) normalized xy and xz, respectively, projections of spatial distribution of absorbed energy (a.u.) due to a 1 nm in diameter 30 keV electron beam incident on the scintillator. Moreover, the corresponding xy and xz projections of five electron trajectories are shown in different colors. Moreover, the level curves containing 25, 50, 70 and 90 % of the absorbed energy are shown in the respective projection.

a nanometer-scale focused electron beam at the scintillator surface. This limitation arises from the fact that the location of the scintillator is approximately 60 cm below the electron gun of the modified SEM. Placing the scintillator screen closer to the electron gun would imply having it inside the specimen chamber, which poses a challenge due to the requirement of an oil immersion medium between the scintillator and the objective lens. Such a medium cannot be used in vacuum conditions, as it would contaminate the microscope chamber.

One way to overcome this challenge might be the use of solid-immersion optics or a more sophisticated isolation of the oil medium within the SEM specimen chamber. Another possibility could be attaching a custom mechanical extension at the bottom of the SEM chamber that extends into the chamber. This would be similar in spirit to a CF tubulated adapter, but instead of extending the tubular length outside the chamber, it would extend into the vacuum volume. This would allow the scintillator screen to be installed in the same configuration used in this work (as a vacuum–air interface window), while positioning it closer to the electron gun, where nanometer-scale focusing of the electron beam is more easily achievable.

7.2.2 Achieving electron number resolving

Following the terminology of [30] and [17], the capability of a photosensor to distinguish zero or one photon will be called photon counting, and the capability of a photosensor to count multiple photon numbers like zero, one, two, three, etc., will be called photon number resolving. In this section, a similar terminology will be used for the electron detector. The capability of the electron detector to distinguish between zero or one electron at the same position of incidence at the scintillator will be called electron counting. The detector presented in this work is capable of doing electron counting. The capability of the electron detector to count multiple electron events, like one, two, three, etc., at the same position of incidence at the scintillator will be called electron number resolving. In what follows, it will be explained how the setup of the electron detector may be modified to attempt achieving electron number resolving.

As reported in Figure 6.2d, the number of detected photons Σ_{ph} per 30 keV electron event is described by a normal distribution with a mean photon number of $\overline{\Sigma_{ph}} = 26$ and a standard deviation of $\sigma_n = 6.4$ photons. This high standard deviation implies that if one has an event with a photon count of 60, then one cannot conclude whether such an event is due to three electron events, each of 20 photon counts, or due to two electron events, each of 30 photon counts, for instance. Thus, one limitation to achieving electron number resolving is this wide range of photon values that can be associated with each electron event. If we can modify the detector setup in such a way that the resulting normal distribution has a small enough standard deviation, then most electron events will have photon values that are very close to each other, in such a way that the probability of a single electron event having the photon count corresponding to two electron events is negligibly small. In order to know how to modify the detector setup, we have to discuss which properties of it are responsible for the value of the standard deviation of the normal distribution.

The number of detected photos Σ_{ph} due to an incident electron is determined by a sequence of probable events. Among them, one can consider the number of scintillated photons, the direction of emission of the scintillated photons, and whether or not the scintillated photons are reflected or transmitted through the many components of the optical system. Of all these, one of the most important influences is the number of scintillated photons per electron event. Furthermore, notice that an important characteristic that influences the number of scintillated photons is the maximum penetration depth of the electron trajectory. One electron could be backscattered promptly, not allowing it to have a deep penetration depth, and as a consequence, this electron just deposited a small amount of its kinetic energy to the scintillator, and as a consequence, the number of scintillated photons is reduced. Or one electron expends all of its kinetic energy inside a small region of the scintillator, maximizing the number of scintillated photons from that small region. To understand the behavior of the possible maximum penetration depths z_{max} of many electron trajectories, Figure 7.2a shows the histogram of the maximum penetration depth z_{max} of the 7×10^5 30 keV electron trajectories in the YAG:Ce scintillator simulated in Chapter 3. The form of the histogram is in good qualitative agreement with the fact that the distribution describing the number of detected

photos Σ_{ph} due to an incident electron is a normal distribution.

One possible modification to the detector setup can be to use a thin enough scintillator so that most of the electron trajectories have a penetration depth much larger than the thickness of the scintillator. As a consequence, most of the electron trajectories that have a maximum penetration depth much larger than the thickness of the scintillator will be such that their initial trajectory segment along the thin scintillator will have a length of around the thickness of the scintillator. Hence, these electron trajectories will deposit approximately the same amount of their kinetic energy into the scintillator, and thus these electron events will scintillate approximately the same number of photons, potentially reducing the width of the distribution describing the number of detected photos Σ_{ph} per electron event. For the simulated 30 keV electron trajectories, the 25 th percentile of the values of maximum penetration depth is 1004.2 nm and is indicated by a vertical red dashed line in Figure 7.2a. Figure 7.2b plots 70 electron trajectories such that their maximum penetration depth z_{max} is above the 25 th percentile value. The vertical axis of the plot is limited to the value of the 25 th percentile of the histogram of maximum penetration depths. It can be seen that the length of many of these trajectories, from the position of incidence till reaching the penetration depth of the 25 th percentile value, is of the order of the thickness of the scintillator.

One good consequence of the fact that the initial segments of these electron trajectories from the position of incidence till reaching the penetration depth of the 25 th percentile value is that due to the stochastic nature of the movement of the electrons in the material, many of these trajectories will occupy disjoint regions of space. This will allow each electron event to produce its scintillated photons with different activators. This can potentially increase the threshold of the maximum number of electrons that can be counted before saturating that region of the scintillator.

The appropriate thickness and material of the scintillator crystal to be used to attempt achieving this goal has to be studied further. One could consider using a host crystal that possesses activators just within the desired region of scintillation. In this way the crystal will possess scintillation properties only in the desired region of space; therefore, one does not have the problem of having to work with a thin (thus fragile) scintillator. Moreover, photons emitted from the scintillation region will always be traveling through the same crystal (this would not be the case if the thin scintillator were hosted by a different transparent material), which can facilitate their propagation through the whole crystal and thus improve their collection.

7.2.3 Collection efficiency and modeling of point spread function

The performance of the optical system is influenced by both its photon collection efficiency and its spatial resolution, which is described by its point spread function (PSF). Therefore, an accurate modeling of these two aspects is essential for a reliable description of the detector optical system.

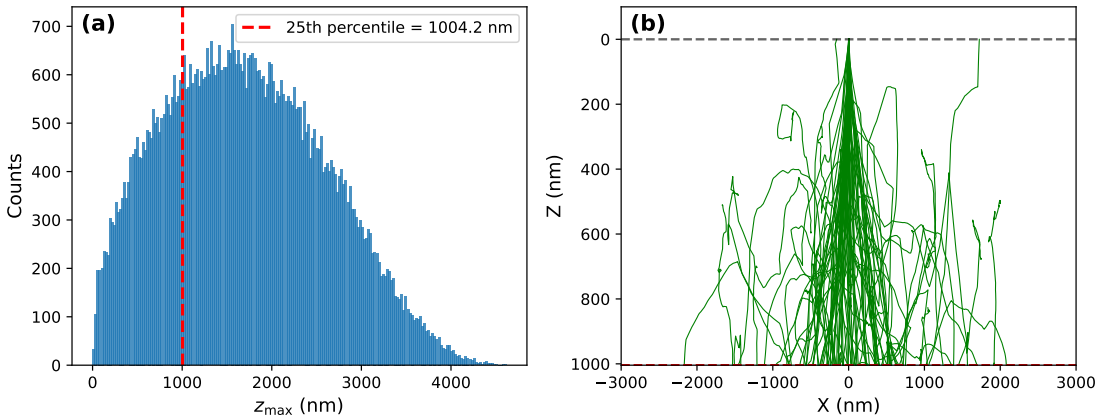

Figure 7.2: Data analysis for 30 keV electron trajectories in the YAG:Ce scintillator: (a) Histogram (light blue) of maximum penetration depth z_{max} of the electron trajectories. The 25 th percentile value is indicated by the vertical red dashed line; (b) Electron trajectories (green lines) with a maximum penetration depth larger than the 25 th percentile. 70 electron trajectories are plotted.

Computation of collection efficiency considering the distribution of emission spectra of the scintillator

In the present work, the collection efficiency of the optical system was evaluated at a single wavelength corresponding to the maximum of the scintillator emission spectrum (see section 4.3.1). While this approximation provides a first estimate of collection efficiency, the scintillation process produces photons over a finite wavelength range. Since the optical properties of the system (e.g., reflectivity and transmission) generally depend on wavelength, a more accurate modeling of the collection efficiency requires taking the emission spectrum of the scintillator into account.

The computation of the collection efficiency of the optical system, considering the distribution of the scintillator's emission spectra, is now explained.

Let $\lambda \mapsto \phi(\lambda)$ be the normalized distribution of emission spectra of the scintillator.

Let $\lambda \mapsto \eta(\lambda)$ be the collection efficiency of the optical system at the wavelength λ.

Then, $\phi(\lambda)d\lambda$ is the fraction of photons that are emitted with a wavelength in the interval $[\lambda, \lambda + d\lambda]$. And $\eta(\lambda)\phi(\lambda)d\lambda$ is the fraction of photons that are collected with a wavelength in the interval $[\lambda, \lambda + d\lambda]$. Thus,

$$\eta = \int_0^\infty \eta(\lambda)\phi(\lambda)d\lambda$$

is the fraction of photons that are collected by the optical system. η is called the collection efficiency of the optical system.

Thus, once the functions ϕ and η are known, the collection efficiency of the optical system η can be calculated as described above.

The above treatment accounts for the spectral dependence of the collection efficiency. However, the present model still relies on an additional assumption, namely that photons are emitted isotropically (see section 4.3.1). In a more realistic description, the angular distribution of the emitted photons should also be considered, as it can influence the fraction of light collected by the optical system. This distribution can be studied by imaging the back focal plane (Fourier plane) of the objective lens.

Modeling of the point spread function of the optical system

The point spread function of the optical system can be modeled using Ansys Zemax OpticStudio© [31]. Furthermore, one may study the imaging of the extended light source arising from the scintillated light around the electron trajectories in the scintillator. This may be complemented by simulations of light propagation inside the scintillator, which can be carried out with the Monte Carlo program LITRANI [32]. LITRANI calculates the path of a photon starting from its production in the crystal by an ionizing event all the way through the different materials until it is absorbed or detected [33].

7.2.4 Implementations with different scintillator materials

The scintillator crystal used for transforming a portion of the kinetic energy of incident electrons into photons that are later detected with a camera is an essential element of this electron detector. Thus, the scintillator properties, such as its photon yield, decay constant, index of refraction, density, and total stopping power, to name a few, play an important role in the characteristics of the detector. For instance, choosing a material with a higher photon yield and density than the YAG:Ce scintillator could potentially increase the signal-to-noise ratio of the electron events and improve the spatial resolution of the detector, respectively. The website `https://scintillator.lbl.gov/` provides a library of organic and inorganic scintillator materials together with their measured scintillation properties and citations to the papers in which the original measurements were reported. This can serve as one reference to find candidates of scintillators that could improve the characteristics of the electron detector presented in this work. Table 7.1 below shows seven commercially available candidates of scintillators, together with some of their properties, that could improve some characteristics of the electron detector. The scintillator crystal employed in this work, namely YAG:Ce, is also shown as a reference.

As pointed out by [34], both the size and shape of the interaction volume of many electron trajectories depend on the atomic number of the materials through which the electrons travel. For high atomic number materials, the interaction volume resembles an oblate spheroid. Its spatial dimensions are smaller and closer to the incidence surface for higher density materials. Examples of these materials are GAGG:Ce and LYSO:Ce and these could potentially increase the signal-to-noise ratio of the electron events and improve the spatial resolution of the detector due to their higher photon yields and densities. For low atomic number materials, the interaction volume resembles a cone hanging down from the surface. This kind of shape of the interaction volume is the one that was explained to be beneficial for electron number resolving in the previous section 7.2.2. An example of

these materials is BC-404.

Table 7.1: Candidate scintillator materials and their properties.

Scintillator	Photon yield (photons/keV)	Density (g/cm^3)	Decay constant (ns)	λ_{max} (nm)	Refractive index	**Source**
			Inorganic			
YAG:Ce	30	4.57	70	550	1.82	[35]
GAGG:Ce	30/54	6.60	50/150	520/530	1.91	[36]
LYSO:Ce	33	7.10	36	420	1.81	[37]
			Plastic			
BC-404	68% Anthracene	1.02	1.8	408	1.58	[38]

Bibliography

[1] Ervin B. Podgorsak. *Radiation Physics for Medical Physicists*. Graduate Texts in Physics. Springer International Publishing, Cham, Switzerland, 3 edition, 2016.

[2] J. B. Birks. *The Theory and Practice of Scintillation Counting*. Pergamon Press, Oxford, UK, 1964.

[3] Glenn F. Knoll. *Radiation Detection and Measurement*. John Wiley & Sons, Hoboken, NJ, 4 edition, 2010.

[4] Luis Alfredo Ixquiac Méndez, Martino Zanetti, Tilman Kräft, and Thomas Juffmann. Low-energy single-electron detector with submicron resolution. *ACS Photonics*, 2025.

[5] Barnaby D. A. Levin. Direct detectors and their applications in electron microscopy for materials science. *Journal of Physics: Materials*, 4(4):042005, July 2021.

[6] X. Llopart, J. Alozy, R. Ballabriga, M. Campbell, R. Casanova, V. Gromov, E. H. M. Heijne, T. Poikela, E. Santin, V. Sriskaran, L. Tlustos, and A. Vitkovskiy. Timepix4, a large area pixel detector readout chip which can be tiled on 4 sides providing sub-200 ps timestamp binning. *Journal of Instrumentation*, 17(01):C01044, January 2022.

[7] Hugh T Philipp, Mark W Tate, Katherine S Shanks, Luigi Mele, Maurice Peemen, Pleun Dona, Reinout Hartong, Gerard van Veen, Yu-Tsun Shao, Zhen Chen, Julia Thom-Levy, David A Muller, and Sol M Gruner. Very-High Dynamic Range, 10,000 Frames/Second Pixel Array Detector for Electron Microscopy. *Microscopy and Microanalysis*, 28(2):425–440, April 2022.

[8] Max T.B. Clabbers, Michael W. Martynowycz, Johan Hattne, Brent L. Nannenga, and Tamir Gonen. Electron-counting microed data with the k2 and k3 direct electron detectors. *Journal of Structural Biology*, 214(4):107886, 2022.

[9] G. McMullan, A. R. Faruqi, and R. Henderson. Chapter One - Direct Electron Detectors. In R. A. Crowther, editor, *Methods in Enzymology*, volume 579 of *The Resolution Revolution: Recent Advances In cryoEM*, pages 1–17. Academic Press, January 2016.

[10] Crytur spol. s r.o. Yag:ce scintillator material, 2025. Accessed: 2025-09-08.

[11] M. C. C. Mihaila, P. Weber, M. Schneller, L. Grandits, S. Nimmrichter, and T. Juffmann. Transverse electron-beam shaping with light. *Physical Review X*, 12:031043, 2022.

[12] Matthias Schneller. Simulation of electron-light interactions. Master's thesis, Universität Wien, 2022. Supervised by Thomas Juffmann.

[13] H. Demers, N. Poirier-Demers, A. Réal Couture, D. Joly, M. Guilmain, N. de Jonge, and D. Drouin. Three-dimensional electron microscopy simulation with the casino monte carlo software. *Scanning*, 33(3):135–146, 2011.

[14] Eduard Aleksanyan, Marco Kirm, Sebastian Vielhauer, and Vachagan Harutyunyan. Investigation of luminescence processes in yag single crystals irradiated by 50 mev electron beam. *Radiation Measurements*, 56:54–57, 2013.

[15] William Feller. *An Introduction to Probability Theory and Its Applications, Volume I.* John Wiley & Sons, New York, NY, USA, 3rd edition, 1971.

[16] James R. Janesick. *Photon Transfer*, volume PM170 of *SPIE Press Monograph*. SPIE Press, The International Society for Optical Engineering, 2007.

[17] Hamamatsu Photonics. qcmos®: Quantitative cmos technology enabled by photon number resolving. White paper, Hamamatsu Photonics.

[18] Michael Hirsch, Richard J. Wareham, Maria L. Martin-Fernandez, Mark P. Hobson, and David J. Rolfe. A stochastic model for electron multiplication charge-coupled devices – from theory to practice. *PLoS ONE*, 8(1):e53671, 2013.

[19] Duncan P. Ryan, Megan K. Dunlap, Martin P. Gelfand, James H. Werner, Alan K. Van Orden, and Peter M. Goodwin. A gain series method for accurate emccd calibration. *Scientific Reports*, 11:18348, 2021.

[20] Daniel Berrar. Performance measures for binary classification. In Shoba Ranganathan, Michael Gribskov, Kenta Nakai, and Christian Schönbach, editors, *Encyclopedia of Bioinformatics and Computational Biology*, pages 546–560. Elsevier, 2019.

[21] Dominique Drouin, Alexandre Réal Couture, Dany Joly, Xavier Tastet, Vincent Aimez, and Raynald Gauvin. Casino v2.42—a fast and easy-to-use modeling tool for scanning electron microscopy and microanalysis users. *Scanning*, 29(3):92–101, 2007.

[22] David C. Joy. *Monte Carlo Modeling for Electron Microscopy and Microanalysis*. Oxford Series in Optical and Imaging Sciences. Oxford University Press, New York, 1995.

[23] KLA Corporation. Filmetrics reflectance calculator, 2025. Accessed: 2025-09-08.

[24] Pedro Andreo, David T. Burns, Alan E. Nahum, Jan Seuntjens, and Frank Herbert Attix. *Fundamentals of Ionizing Radiation Dosimetry*. Wiley-VCH, Weinheim, 2017.

[25] M.J. Berger, J.S. Coursey, M.A. Zucker, and J. Chang. Estar: Stopping power and range tables for electrons. Online database, National Institute of Standards and Technology, 2017.

[26] Hamamatzu. qCMOS cameras | Hamamatsu Photonics.

[27] Stefan van der Walt, Johannes L. Schönberger, Juan Nunez-Iglesias, François Boulogne, Joshua D. Warner, Neil Yager, Emmanuelle Gouillart, Tony Yu, and the scikit-image contributors. scikit-image: Image processing in python. *PeerJ*, 2:e453, 2014.

[28] Hamamatsu Photonics K.K. *ORCA-Quest 2 (C15550-22UP) Instruction Manual*. Hamamatsu Photonics K.K., 2024. Accessed: 2026-05-11.

[29] Guozhang Lin. Sum of poisson-distributed random variables, 2021. Course report for SML: Probability.

[30] Hamamatsu Photonics. Orca-quest qcmos camera c15550-20up technical note. Technical Report SCAS0154E, Hamamatsu Photonics K.K., May 2022. Accessed: 2026-02-17.

[31] Ansys Inc. Ansys zemax opticstudio, 2026. Optical design and simulation software.

[32] François-Xavier Gentit. Litrani: a general purpose monte-carlo program simulating light propagation in isotropic or anisotropic media. *Nuclear Instruments and Methods in Physics Research Section A*, 486(1–2):35–39, 2002.

[33] Arno Knapitsch. *Photonic crystals: enhancing the light output of scintillation based detectors*. Phd thesis, Technische Universität Wien, 2012.

[34] David C. Joy. An introduction to monte carlo simulations. *Scanning Microscopy*, 5(2):329–337, 1991. Article 4.

[35] Yag:ce scintillator. `https://www.crytur-usa.com/materials/yagce/`. Accessed: 2026-02-19.

[36] Gagg:ce scintillator. `https://www.epic-crystal.com/scintillation-crystals/gaggce-crystal.html`. Accessed: 2026-02-19.

[37] Lyso:ce scintillator. `https://luxiumsolutions.com/radiation-detection-scintillators/crystal-scintillators`. Accessed: 2026-02-19.

[38] Bc-404 plastic scintillator. `https://luxiumsolutions.com/radiation-detection-scintillators/plastic-scintillators`. Accessed: 2026-02-19.